Supplementary Information for

Design of proteasome inhibitors with oral efficacy *in vivo* against *Plasmodium falciparum* and selectivity over the human proteasome

Stanley C. Xie[1#], Riley D. Metcalfe[1#], Hirotake Mizutani[2#], Tanya Puhalovich[1], Eric Hanssen[1,3], Craig J. Morton[1], Yawei Du[1], Con Dogovski[1], Shih-Chung Huang[2], Jeffrey Ciavarri[2], Paul Hales[2], Robert J. Griffin[2], Lawrence H. Cohen[2], Bei-Ching Chuang[2], Sergio Wittlin[4, 5], Ioanna Deni[6], Tomas Yeo[6], Kurt E. Ward[6], Daniel C. Barry[1], Boyin Liu[1], David L. Gillett[1], Benigno F. Crespo-Fernandez[7], Sabine Ottilie[8], Nimisha Mittal[8], Alisje Churchyard[9], Daniel Ferguson[10], Anna Caroline C. Aguiar[11], Rafael V.C. Guido[11], Jake Baum[9], Kirsten K. Hanson[10], Elizabeth A. Winzeler[8], Francisco-Javier Gamo[7], David A. Fidock[6,12], Delphine Baud[13], Michael W. Parker[1,14], Stephen Brand[13], Lawrence R. Dick[1,15¥], Michael D.W. Griffin[1¥], Alexandra E. Gould[2¥*], Leann Tilley[1 ¥*]

[1]Department of Biochemistry and Pharmacology, Bio21 Molecular Science and Biotechnology Institute, The University of Melbourne, Melbourne, VIC 3010, Australia; [2]Discovery Strategy and Operations, Takeda Pharmaceuticals International Co., Cambridge, Massachusetts 02139, USA; [3]Ian Holmes Imaging Centre, Bio21 Institute, The University of Melbourne, Melbourne, VIC 3010, Australia; [4]Department of Medical Parasitology and Infection Biology, Swiss Tropical and Public Health Institute, 4051 Basel, Switzerland, [5]University of Basel, 4003 Basel, Switzerland; [6]Department of Microbiology & Immunology, Columbia University Irving Medical Center, New York, NY 10032, USA; [7]Global Health Pharma Research Unit, GSK, Severo Ochoa, 28760-Tres Cantos (Madrid), Spain; [8]Department of Pediatrics, School of Medicine, University of California, San Diego, La Jolla, California 92093, USA; [9]Department of Life Sciences, Imperial College London, London SW7 2AZ, UK; [10]Department of Biology and South Texas Center for Emerging Infectious Diseases, University of Texas at San Antonio, Texas, TX 78249, USA; [11]São Carlos Institute of Physics, University of São Paulo, São Carlos, SP, 13563-120, Brazil; [12]Division of Infectious Diseases, Department of Medicine, Columbia University Irving Medical Center, New York, NY 10032, USA; [13]Drug Discovery, Medicines for Malaria Venture, 1215, Geneva 15, Switzerland; [14]Structural Biology, St. Vincent's Institute of Medical Research, Fitzroy, VIC 3065, Australia; [1,15]Seofon Consulting, Natick, Massachusetts 01760, USA

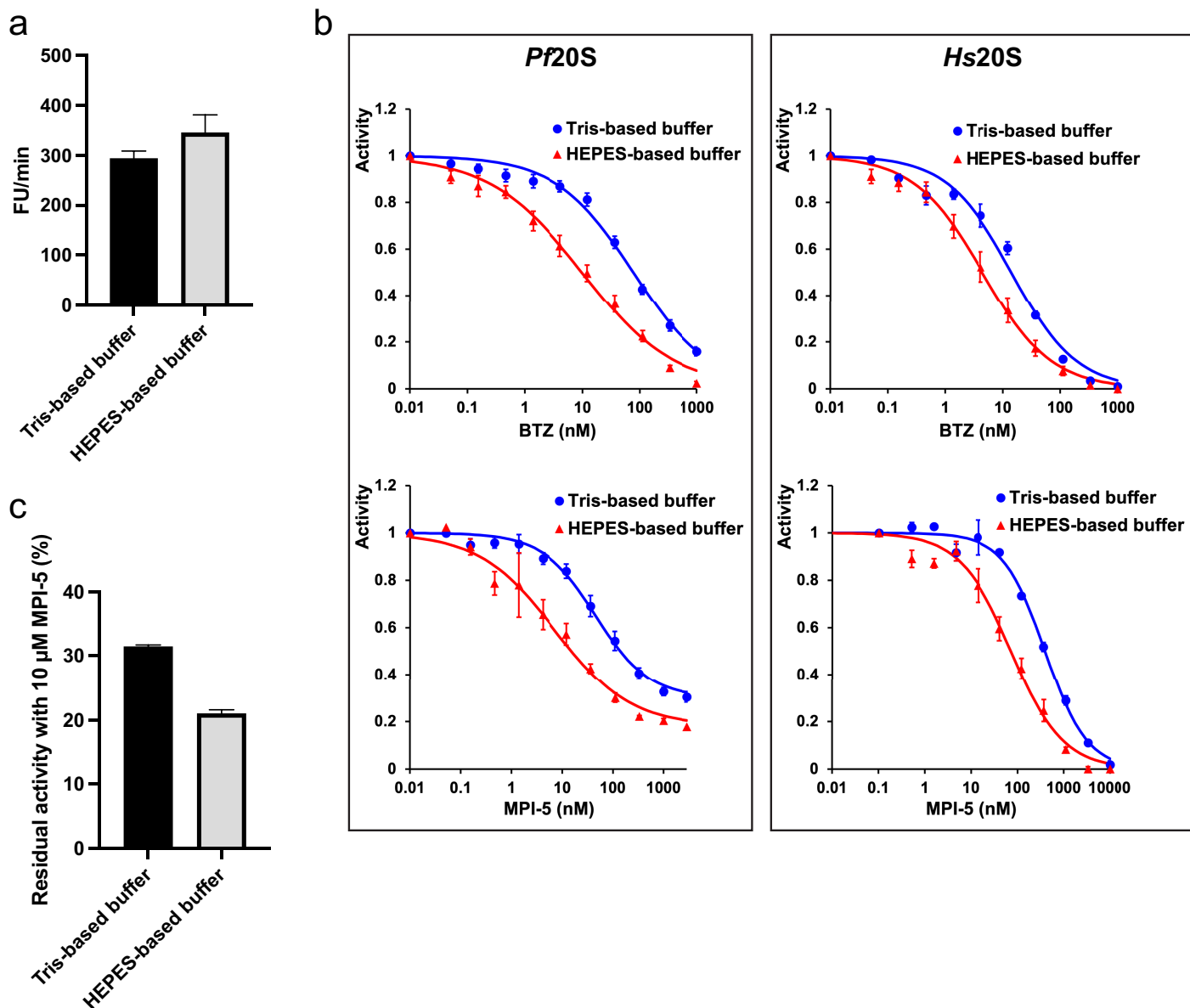*For correspondence. Alexandra E. Gould: sandy.gould@takeda.com (Chemistry) and Leann Tilley: ltilley@unimelb.edu.au (Biology)

This PDF file includes:

Figures S1 to S8

Tables S1 to S10

**Supplementary Methods, including chemical synthesis and characterization**

SI References

Fig. S1. HEPES-based buffer permits more efficient inhibition of *Pf*20S than Tris-based buffer. (a) *Pf*20S β5 and *Hs*20S β5c cleavage of the fluorogenic substrate, Ac-WLA-AMC, was assayed in the presence of human PA28αβ, in 50 mM Tris pH 7.4, 5 mM MgCl$_2$, 1 mM DTT, 0.01% BSA or 20 mM HEPES pH 7.4, 0.5 mM EDTA, 0.01% BSA at 37°C. *Pf*20S β5 and *Hs*20S β5c activities were similar in the two buffer systems. Error bars represent SEM from three independent assays. (b) Inhibition of *Pf*20S and *Hs*20S activities by MPI-5 and bortezomib (BTZ) in the presence of HEPES- and Tris-based buffers. The peptide boronates were consistently 2 to 8 times more potent in the HEPES-based buffer compared with the Tris-based buffer against both *Pf*20S β5 and *Hs*20S β5c activity. See Table S1. Data shown are average curves generated from 2-8 independent assays. Error bars correspond to half of the range or SEM. (c) Effects of different buffer components on residual activity following inhibition of *Pf*20S β5 activity by 10 μM MPI-5. MPI-5 did not completely inhibit cleavage of Ac-WLA-AMC, even at high concentrations, likely due to some level of cleavage of Ac-WLA-AMC by *Pf*20S β2 (1, 2). Error bars represent SEM from three independent assays.

a

b

c   *Pf*20S
MPI-5

*Pf*20S
BTZ

d   *Hs*20S
MPI-5
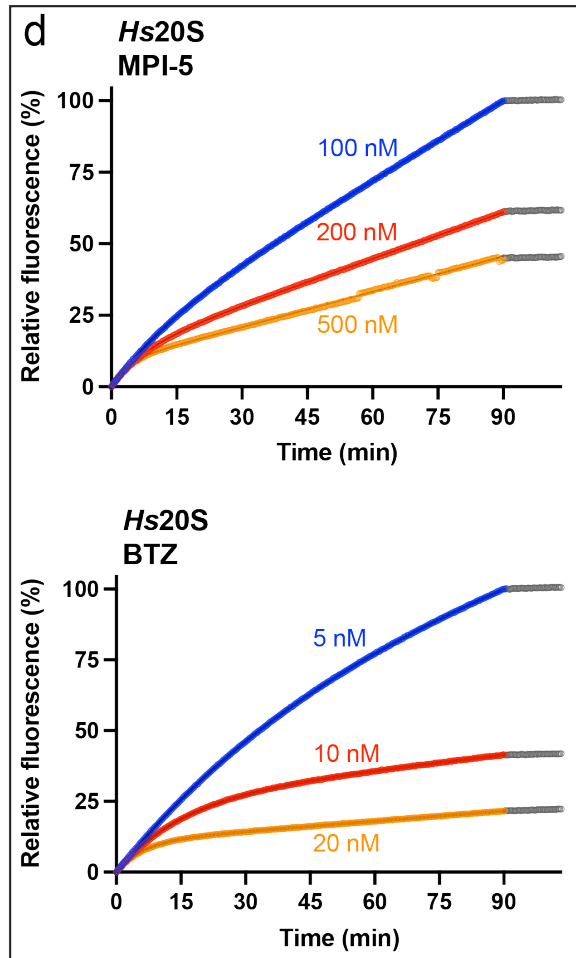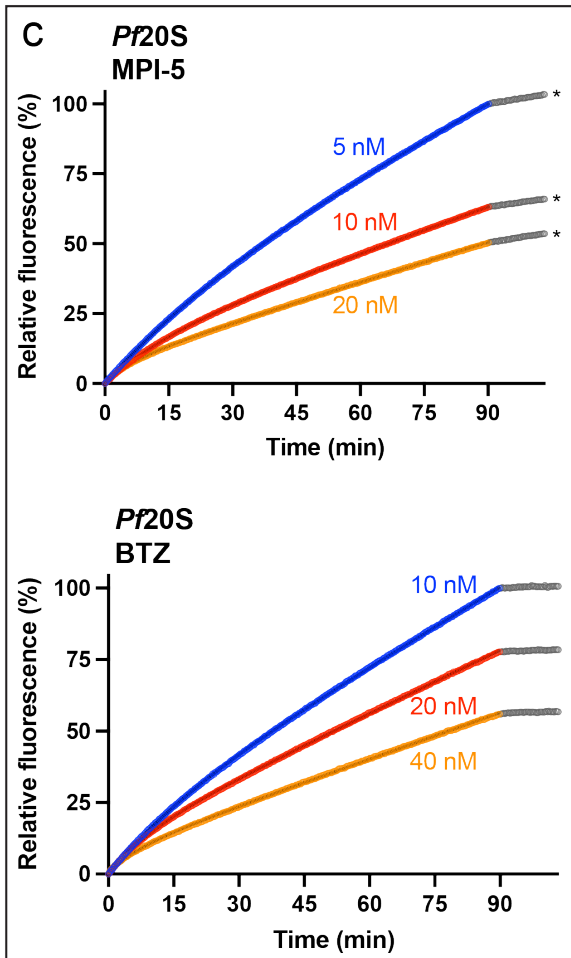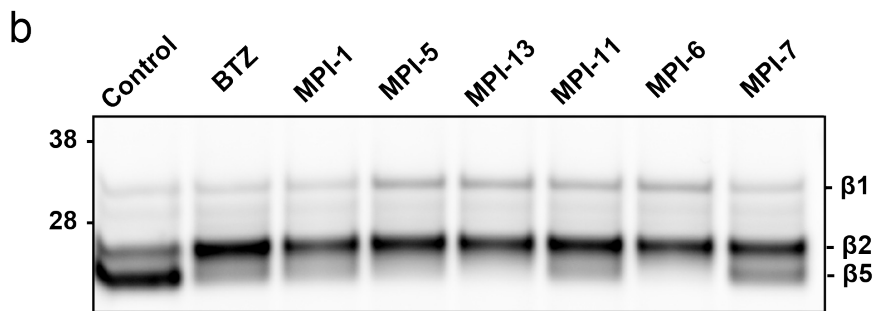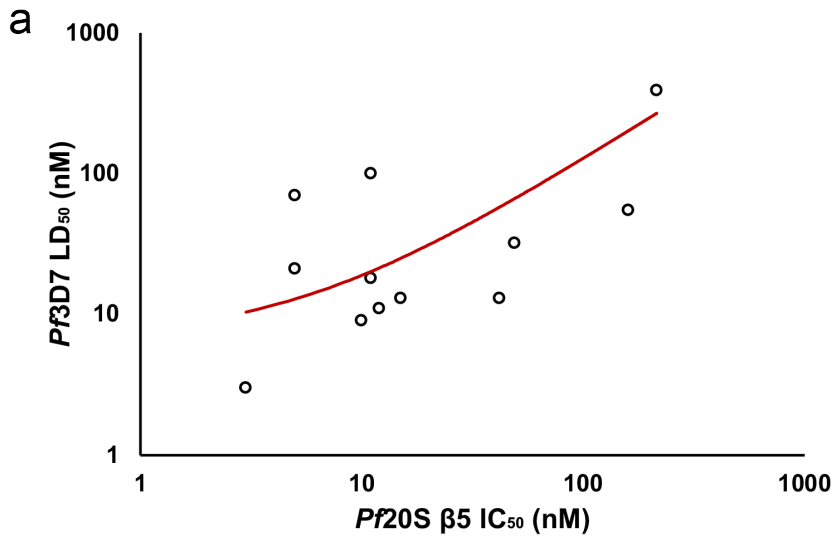
*Hs*20S
BTZ

Fig. S2. Correlation of cellular and biochemical assays and analysis of binding to the *Pf*20S β5 and *Hs*20S β5c active sites. (a) Correlation plot of the activities of the compound set in *Pf*20S β5 and *Pf* 3D7 assays. A linear regression trendline is depicted in red. $R^2 = 0.61$. (b) Purified *Pf*20S proteasome was incubated with selected compounds for 2 h, and then with the activity probe, BMV037, for 2 h. Gel scans reveal subunits that remain active after treatment. The image shown is representative of three independent experiments. (c, d) Representative progress curves of proteasome-catalyzed Ac-WLA-AMC hydrolysis at varying concentrations of bortezomib (BTZ) and MPI-5 demonstrating slow-binding (time-dependent) inhibition of human and *P. falciparum* proteasome β5 active sites. The progress curves were monitored for 90 min in the presence of the inhibitor at the concentrations indicated in the figure. After 90 min, the residual proteasome activity at a saturating inhibitor concentration (i.e., 5 µM bortezomib or 10 µM MPI-5) was monitored for an additional 10 min. *Pf*20S exhibited residual activity (14% of the total uninhibited activity) in the presence of 10 µM MPI-5 as indicated by asterisks. This residual activity of *Pf*20S likely results from hydrolysis of Ac-WLA-AMC in the *Pf*20S β2 active site and can be inhibited by high concentrations of bortezomib. Progress curves such as these were analysed as described in the Materials and Methods to generate the data plotted in Fig. S3.
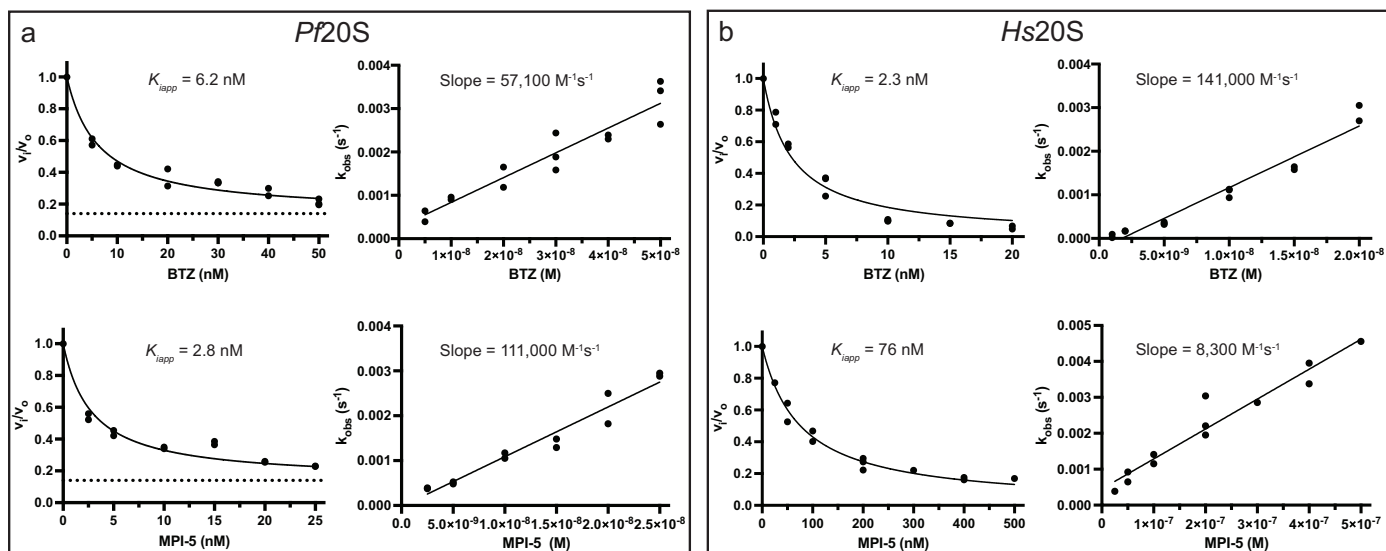
Fig. S3. Estimation of kinetic parameters for MPI-5 and bortezomib (BTZ) binding to *Pf*20S (a) and *Hs*20Sc (b) proteasome β5 active sites. Plots of the final steady-state inhibited reaction velocity divided by the uninhibited reaction velocity (v_i/v_o) as a function of inhibitor concentration were fit as described in the Materials and Methods to estimate apparent *Ki* values (K_{iapp}). Dotted lines represent residual activity of *Pf*20S (14% of the total uninhibited activity). Plots of the rate constant (k_{obs}) for approach to steady state inhibition (derived from the progress curve analysis in Fig. S2c,d) as a function of inhibitor concentration were subject to linear regression to obtain the slope (= k_{off}/K_{iapp}). 12 or 14 progress curves were measured over the indicated concentration range in 3 or 4 independent experiments for each of the enzyme-inhibitor combinations. Kinetic parameters calculated from the analyses are summarized in Table S4.
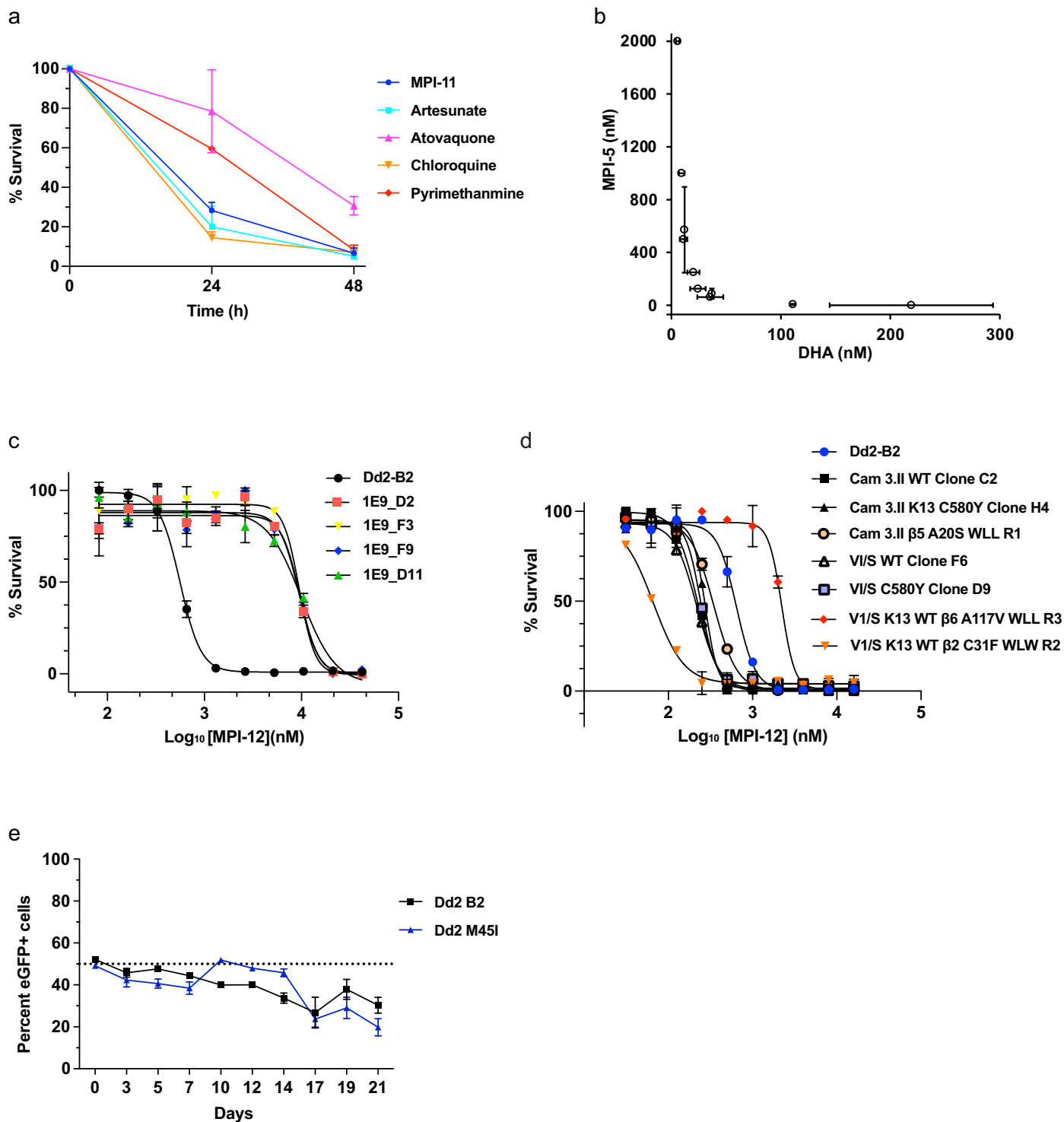
Fig. S4. Kinetics of *P. falciparum* (3D7) growth inhibition and analysis of resistance to amino-amide boronates. (a) 3D7 parasite cultures were treated for 24 or 48 h with MPI-11 or reference compounds with a fast-killing profile (artesunate and chloroquine), a moderate killing profile (pyrimethamine) or a slow killing profile (atovaquone), at 10 times their respective $IC_{50(72h)}$ values. Viability was measured in the subsequent trophozoite stage. (b) Interaction analysis for MPI-5 and DHA. Cam3.II (DHA-resistant) parasites at early ring stage (0-8 h post-invasion (p.i.)) were subjected to 3-h pulses in the presence of different combinations of DHA and MPI-5. Values are plotted for the MPI-5/DHA pair at the 50% $LD_{50(3h)}$ level. Thus, the x and y

axes labels refer to the concentrations of DHA and MPI, respectively, that, in combination, give 50% inhibition. Error bars correspond to SEM from three independent experiments. (c) Dd2-B2 parasites were exposed to MPI-12 at a concentration equivalent to 4.4 x $IC_{50(72h)}$. Cloned recrudescent parasites exhibited $IC_{50(72h)}$ and $IC_{90(72h)}$ increases of ~14-fold to ~19-fold relative to the Dd2-B2 parental line. IC_{50} values generated from three independent assays with technical duplicates are provided in Table S5. One representative assay is shown. (d) Cross-resistance assays with artemisinin-resistant or proteasome-resistant lines. The names designate the K13 status as being mutant (artemisinin-resistant) or wild-type (sensitive). Proteasome-resistant lines were selected using WLW-vs or WLL-vs (harbouring C31F mutation in Pf20S β2 or a A117V mutation in Pf20S β6, respectively). WLW-selected parasites exhibited a 2-fold increase in susceptibility to MPI-12, whereas WLL-vs-selected parasites exhibited an 8-fold decrease in sensitivity to MPI-12. One representative assay is shown and the IC_{50} values are provided in Table S5. (e) The fitness of the 1E9-D2 line was compared to a Dd2-B2 control though mixed culture competition assays with an eGFP-positive Dd2 reporter line (3). Data represent the average of two independent experiments, each with three technical replicates.
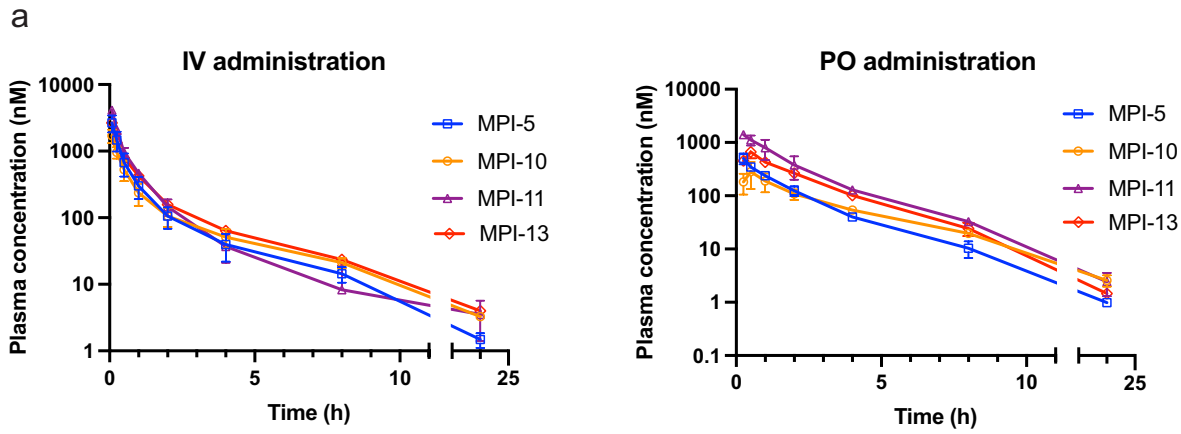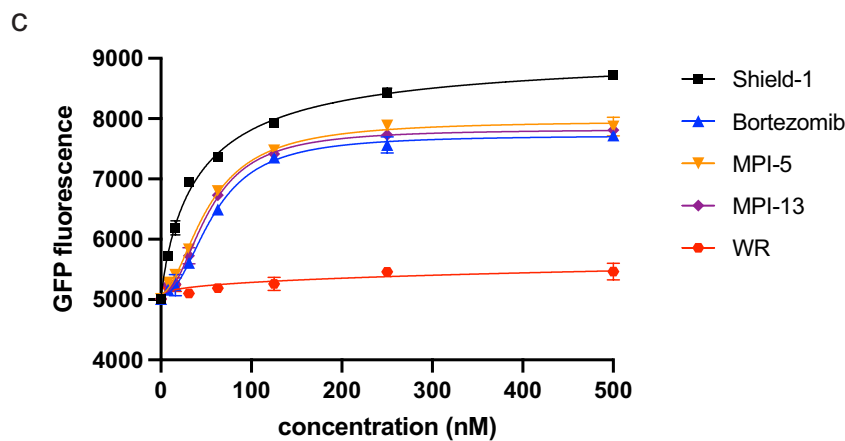
Fig. S5. Rat PK data for selected compounds and validation of on-target activity. (a) MPI-5, MPI-10, MPI-11 and MPI-13 were dosed IV and PO at 1 mg/kg and plasma and blood samples were collected for analysis. (b) Activities of selected compounds against Pf20S β5 M45I mutant. Data represent the mean ± SEM from three independent experiments. (c) GFP-DD reporter assay. GFP-DD transfectants were treated with indicated compounds for 3 h and GFP fluorescence was measured by flow cytometry. Data are the mean ± range/2 of technical duplicates from one representative assay out of three independent experiments.
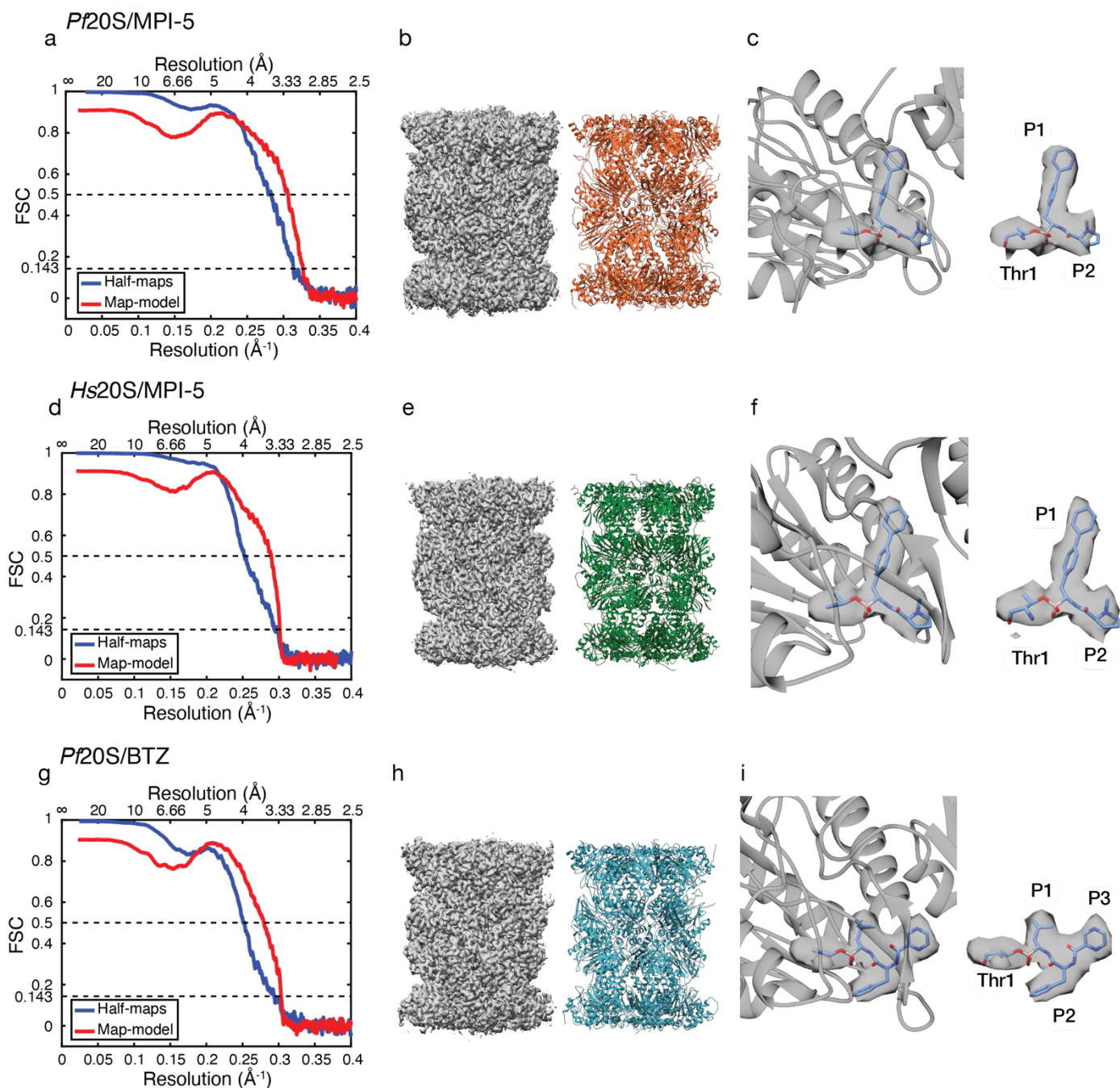
Fig. S6. Resolution estimation, density maps and modelled structures for *Pf*20S and *Hs*20Sc in complex with bortezomib or MPI-5. Cryo-EM data for *Pf*20S/MPI-5 (a-c), *Pf*20S/bortezomib (d-f) and *Hs*20Sc/MPI-5 (g-i). (a,d,g) Gold standard half-map and map-model FSC curves. (b,e,h) Cryo-EM density maps (contoured at 5 σ), alongside ribbon representations of the structures. (c,f,i) Representative cryo-EM density (contoured at 3 σ) for the inhibitors, with ribbon representation of the surrounding β5 subunit.
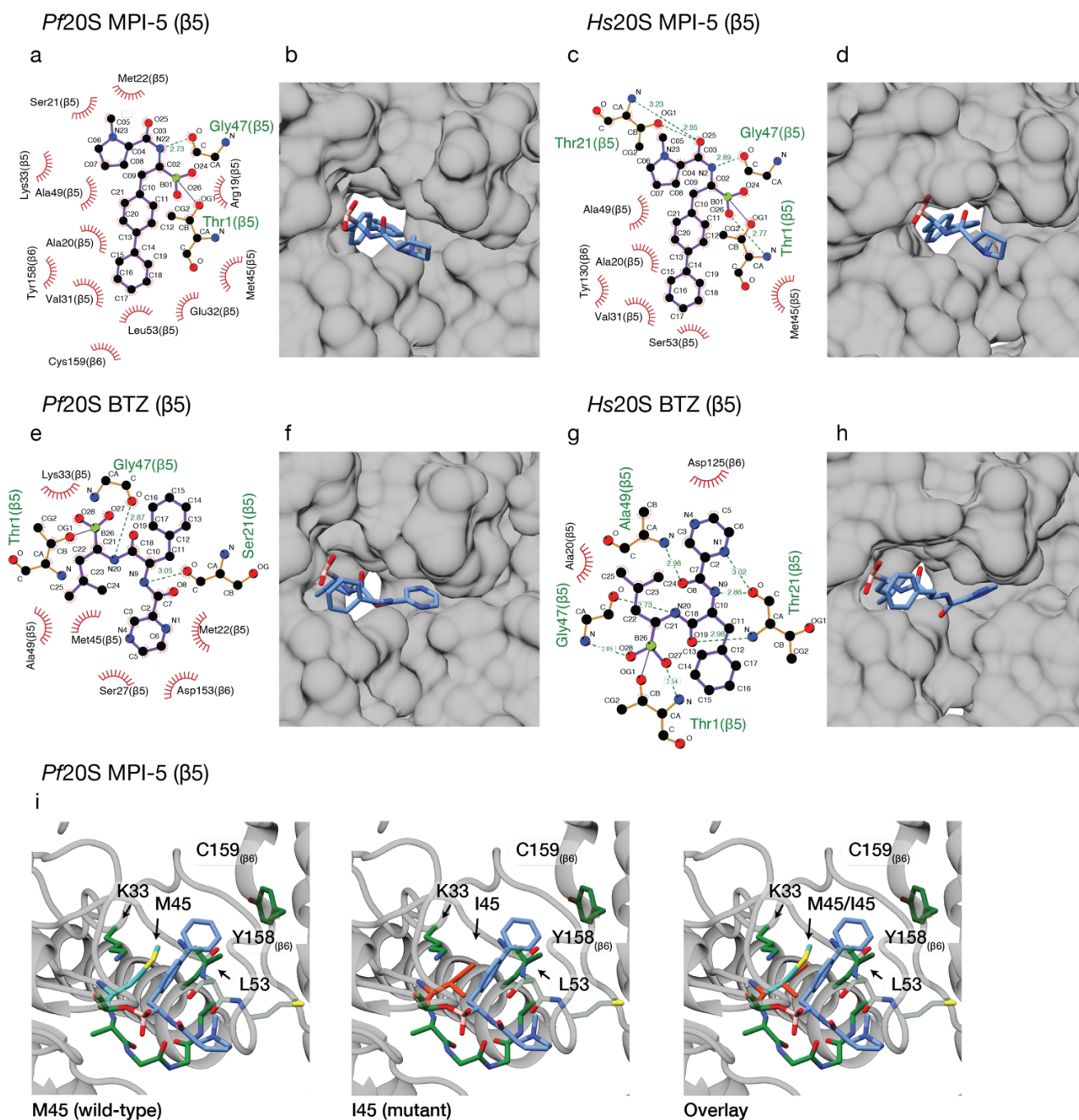
Fig. S7. Maps of interactions and solvent accessible surfaces at the inhibitor/active site interfaces and overlay of wildtype and *Pf*20S β5/ Met145Ile mutant. (a,c,e,g) LigPlot maps of interacting residues for *Pf*20S β5/ MPI-5 (a), *Hs*20S β5c/ MPI-5 (b), *Pf*20S β5/ bortezomib (e) and *Hs*20S β5c/ MPI-5 (g). The H-bonds are indicated with dashed lines. The hydrophobic interactions are indicated with red semi-circles. (b,d,f,h) Solvent accessible surface of the β5 active site for *Pf*20S β5/ MPI-5 (b), *Hs*20S β5c/ MPI-5 (d), *Pf*20S β5 /bortezomib (f) and *Hs*20S β5c/ bortezomib (h), illustrating the more enclosed hydrophobic pocket occupied by MPI-5 in *Pf*20S β5 compared with *Hs*20S β5c. The locations of *Pf*Met22 and *Hs*Ala22 are arrowed. (i) Inhibitor/active site interface for the *Pf*20S β5/ MPI-5 structure (with Met45 depicted in turquoise, left panel), a model of the *Pf*20S β5/ Met145Ile mutant (Ile45 depicted in red; middle panel) and overlay of the two (right panel).
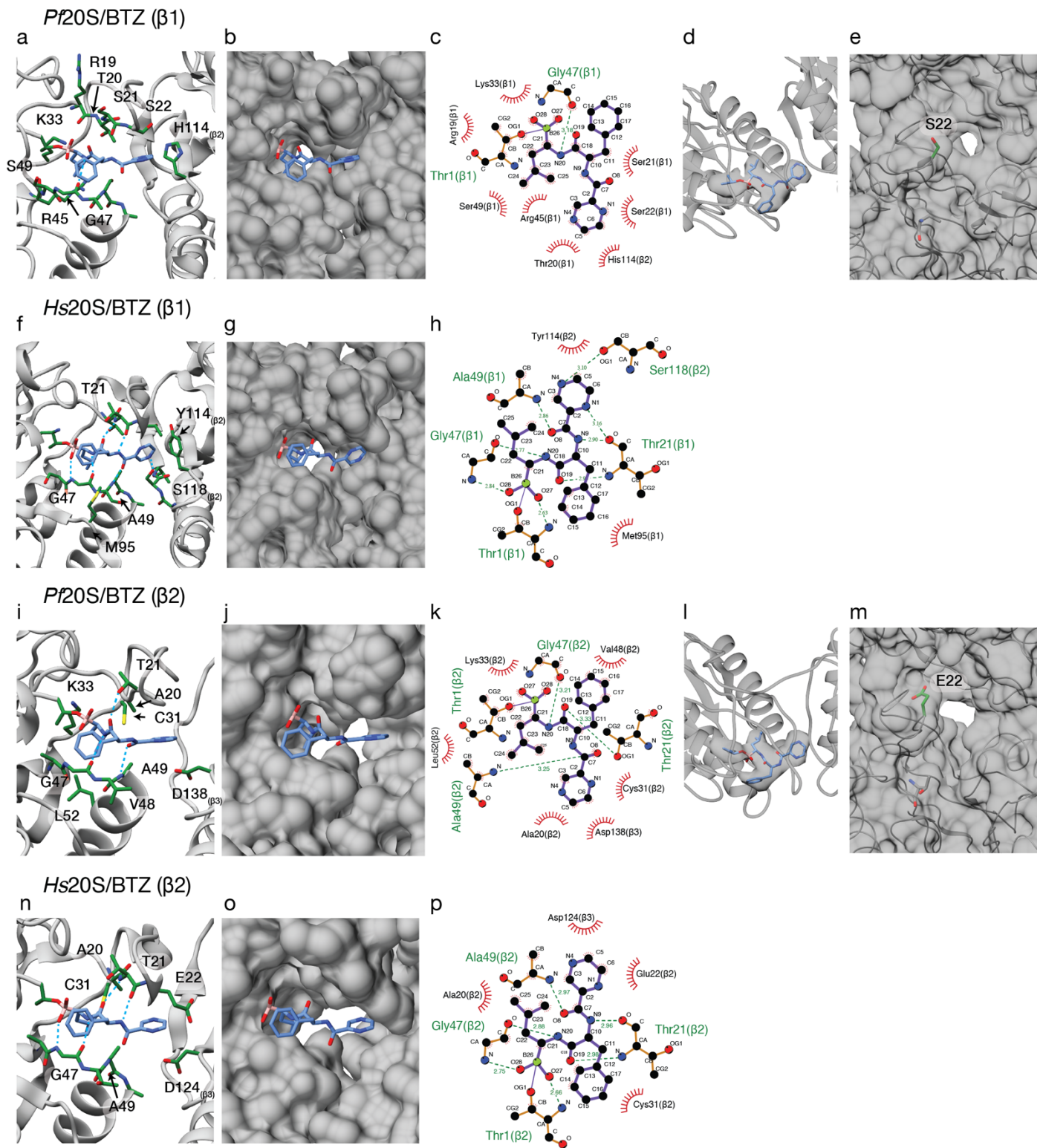
Fig. S8. Structures of *Pf*20S and *Hs*20Sc β1 and β2 active sites with bound bortezomib. Ribbon representations (a,f,i,n), solvent accessible surfaces (b,g,j,o) and LigPlots (c,h,k,p) for bortezomib in the β1 (a-h) and β2 (i-p) subunits of *Pf*20S (a-e,i-m) and *Hs*20Sc (f-h, n-p). (d,l) Representative cryo-EM density (contoured at 3 σ).

Supplementary Tables

Table S1. Inhibitory activities of bortezomib and MPI-5 against purified *P. falciparum* and human 20S proteasome. IC_{50} values for the compound set against Pf20S β5 and Hs20S β5c activity. For MPI-5, IC_{50} values against Pf20S β5 are the concentrations resulting in 50% inhibition of the total inhibitable activity. Data represent the mean ± SEM. n is the number of independent experiments.

Compound	Hs20S β5c IC_{50} (nM) (Tris buffer) [Residual activity][b]	Hs20S β5c IC_{50} (nM) (HEPES buffer) [Residual activity][b]	Fold-difference (IC_{50} Tris/ IC_{50} HEPES)
Bortezomib	14 ± 1 (n = 3) [1 ± 1%]	6 ± 3 (n = 8)[a] [0%]	2.3
MPI-5	410 ± 20 (n = 3) [30 ± 2%]	85 ± 15 (n = 5)[a] [8 ± 1%]	4.8
Compound	Pf20S β5 IC_{50} (nM) (Tris buffer) [Residual activity][b]	Pf20S β5 IC_{50} (nM) (HEPES buffer) [Residual activity][b]	Fold-difference (IC_{50} Tris/ IC_{50} HEPES)
Bortezomib	80 ± 10 (n = 4) [16 ± 2%]	11 ± 3 (n = 7)[a] [2 ± 1%]	7.3
MPI-5	40 ± 10 (n = 4) [31 ± 2%]	5 ± 2 (n = 4)[a] [20 ± 0.4%]	8

[a]Same data sets presented in Tables 1 & S1. [b]Residual activity was measured at 1 μM inhibitor.

Table S2. Physicochemical and ADME characterization of selected compounds. ALogP values were calculated using D360 (Certara, New Jersey, USA).

	ALogP	Solubility (μM)	Caco2 Papp (x10⁻⁶ cm/s) (A to B, B to A)	S9 hepatic extraction ratio (H, R)
Bortezomib	2.2	50		
MPI-1	-0.34	100		
MPI-5	2.5	>200	13, 14	0.8, <0.2
MPI-6	1.3	50		
MPI-7	0.86	>200		
MPI-8	2.1	100	3.6, 12	
MPI-9	1.6	>200	0.54, 4.9	<0.08, <0.2
MPI-10	2.9	>200	8.4, 24	
MPI-11	2.6	>200	18, 22	0.8, 0.2
MPI-12	3.0		17, 25	0.6, 0.2
MPI-13	3.7	67	4.6, 25	0.5, <0.2
MPI-14	3.7			

Table S3. Inhibitory activities of selected compounds against purified *P. falciparum*, human 20S constitutive and immuno proteasome β1 and β2 activities. Mean ± SEM values are provided where relevant.

Compound ID	*Plasmodium falciparum* 20S Proteasome IC$_{50}$ (µM)		*Homo sapiens* 20S constitutive proteasome IC$_{50}$ (µM)		*Homo sapiens* 20S immuno proteasome IC$_{50}$ (µM)	
	β1	β2	β1c	β2c	β1i	β2i
Bortezomib[a]	0.32 ± 0.08	1.6 ± 0.3	0.09 ± 0.02	1.2 ± 0.1	0.005 ± 0.002	0.54 ± 0.08
MPI-1[a]	3.19 ± 0.04	> 10	3.4 ± 0.9	> 10	0.008 ± 0.002	> 10
MPI-5	> 10	> 10	> 10	> 10	> 10	> 10
MPI-6	> 10	> 10	> 2.2/2.2	> 4.9/4.9	0.44	2.9
MPI-7	> 10	> 10	> 10	> 10	0.18	> 10
MPI-8	> 10	> 10	> 10	> 10	> 10	> 10
MPI-9	> 10	> 10	> 10	> 10	6.3 ± 2.1	> 10
MPI-10	> 10	> 10	> 10	> 10	> 10	> 10
MPI-11	> 10	> 10	> 10	> 10	> 10	> 10
MPI-12	> 10	> 10	> 10	> 10	> 10	> 10
MPI-13	> 10	> 10	> 10	> 10	> 10	> 10
MPI-14	> 10	> 10	> 10	> 10	> 10	> 10

[a]Data from (4).

Table S4. Estimated kinetic parameters for the binding of MPI-5 and bortezomib to the *Pf*20S β5 and *Hs*20S β5c active sites.

Compound	*Pf*20S			*Hs*20Sc		
	K_i^a (nM)	k_{off} $(s^{-1})^b$ $t_{1/2}$	k_{on}^c $(M^{-1}s^{-1})$	K_i (nM)	k_{off} (s^{-1}) $t_{1/2}$	k_{on} $(M^{-1}s^{-1})$
MPI-5	1.4	3.1×10^{-4} *37 min*	22×10^4	38	6.3×10^{-4} *18 min*	1.7×10^4
Bortezomib	3.1	3.6×10^{-4} *32 min*	11×10^4	1.1	3.2×10^{-4} *36 min*	28×10^4

$^a K_i$ was calculated as $K_{iapp}/2$ assuming simple competitive inhibition

$^b k_{off}$ was calculated as slope x K_{iapp} from Fig. S3; $t_{1/2} = ln2/k_{off}$

$^c k_{on}$ was calculated as k_{off}/K_i

Table S5. Activities of selected compounds against drug resistant strains, field strains and extraerythrocytic and transmissible forms

Activity of MPI-11 against different parasite lines	
Strain (Sensitivity profile)	IC$_{50}$ value (nM) (number of experiments)
7G8 (Decreased sensitivity to chloroquine)	100/61 (n = 2)
Cam3.1 (Decreased sensitivity to artemisinin)	157 ± 52 (n = 5)
Dd2 (Decreased sensitivity to chloroquine)	126 ± 45 (n = 5)
Dd2 048 (Decreased sensitivity to phosphatidylinositol 4-kinase (PI4K) inhibitor, MMV048)	93/195 (n = 2)
Dd2 DDD107498 (Decreased sensitivity to translation elongation factor 2 (eEF2) inhibitor, DDD107498)	113/84 (n = 2)
Dd2 DSM265 (Decreased sensitivity to dihydroorotate dehydrogenase inhibitor, DSM265)	143 ± 41 (n = 3)
Dd2 GNF156 (Decreased sensitivity to GNF156 (ganaplacide))	143 ± 41 (n = 3)
Dd2 ELQ300 (Decreased sensitivity to cytochrome bc1 inhibitor, ELQ300)	116 ± 51 (n = 5)
K1 (Decreased sensitivity to chloroquine)	141 ± 102 (n = 6)
TM90C2B (Decreased sensitivity to atovaquone)	102/87 (n = 2)
NF54 (Sensitive)	172 ± 87 (n = 5)
Activity of MPI-12 against MPI-12-selected recrudescent parasites	
Parasite line	IC$_{50}$ value (nM) (n = 3)
Dd2-B2 (Wildtype parent)	557 ± 23
1E9_D2 clone	7730 ± 880
1E9_D11 clone	8050 ± 960
1E9_F3 clone	8220 ± 650
1E9_F9 clone	8480 ± 560
Activity of MPI-12 against artemisinin-resistant or proteasome-resistant parasites	
Parasite line (Resistance phenotype)	IC$_{50}$ value (nM) (n = 3)
Dd2-B2 (Wildtype)	454 ± 109
Cam 3.II WT Clone C2 (Wildtype)	293 ± 46

Cam 3.II K13 C580Y Clone H4 (Artemisinin resistant)	348 ± 40
Cam 3.II β5 A20S WLL R1 (WLL-vs resistant)	439 ± 47
V1/S WT Clone F6 (Wildtype)	341 ± 65
V1/S C580Y Clone D9 (Artemisinin resistant)	324 ± 47
V1/S K13 WT β2 C31F WLW R2 (WLW-vs resistant)	145 ± 40
V1/S K13 WT β6 A117V WLL R3 (WLL-vs resistant)	3420 ± 1200
Activities against Brazilian field isolates of *P. falciparum*	
Assay [Compound]	Effect (nM)
P. falciparum (5) [MPI-10]	median 18 nM; range: 7-134 (n = 7)
P. vivax (5) [MPI-10]	median 34 nM; range: 7-68 (n = 9)
Activities of selected compounds in field, transmission and exoerythrocytic stage assays	
Assay [Compound]	Effect (μM)
Dual gamete formation assay (6) [MPI-11]	$IC_{50(48h)} = 0.68 \pm 0.04$ (n = 4)
Dual gamete formation assay (6) [MPI-13]	$IC_{50(48h)} = 1.0 \pm 0.3$ (n = 4)
Exoerythrocytic sporozoite infection - *P. berghei* (7) [MPI-11]	$IC_{50(48h)} = 0.11 \pm 0.01$ (n = 2; half range)
Exoerythrocytic liver schizont biomass *P. berghei* (7) [MPI-11]	$IC_{50(48h)} = 0.26 \pm 0.05$ (n = 2; half range); 98% reduction
Hepatic merozoite formation - *P. berghei* (7) [MPI-11]	$IC_{50(72h)} = 0.15 \pm 0.02$ (n = 2; half range)
HepG2 growth inhibition in exoerythrocytic stage assay (7) [MPI-11]	$IC_{50(72h)} = 1.35 \pm 0.15$ (n = 2; half range).
P. falciparum NF54 schizont development in primary human hepatocytes (8) [MPI-11]	$IC_{50(96h)} = 0.12 \pm 0.07$ (n = 2; half range)
Primary human hepatocyte toxicity [MPI-11]	$IC_{50(96h)} >10$ (n = 2)

Table S6. Whole-genome sequencing metrics for the MPI-12-resistant clones.

Clones		1E9 D2	1E9 F3	1E9 F9	1E9 D11
Total reads		6,512,929	4,172,657	3,653,328	3,934,593
# Mapped reads		5,724,246	3,069,320	2,588,097	3,025,357
Duplication rate		37.7%	34.0%	31.2%	32.9%
General error rate		2.2%	2.2%	2.2%	2.2%
Mean mapping quality (Phred)		56.1	56.0	55.9	56.0
Read length	min	30	30	30	30
	mean	263.9	272.4	270.2	273.7
	max	301	301	301	301
Insert size	p25	261	227	239	237
	median	346	332	338	349
	p75	443	433	437	454
Depth of coverage	mean	61.30	31.12	31.07	26.41
	SD	154.2	77.3	79.4	64.3
% of *Pf* genome with > x reads	1×	96.4%	96.0%	96.1%	95.9%
	5×	95.1%	94.0%	94.0%	93.5%
	10×	94.1%	91.0%	90.8%	88.8%
	30×	86.3%	49.5%	49.9%	33.1%

Table S7. Identification of point mutations in the *Pf*20S β5 subunit in MPI-12-resistant clones.

Sample	Chromosome	Position	Ref	Alt	Amino acid change	Codon change	Gene name	Description
1E9 D2	Pf3D7_10_v3	441641	C	T	M45I[a]	atG/atA	PF3D7_1011400	proteasome subunit β5
1E9 F3	Pf3D7_10_v3	441641	C	T	M45I	atG/atA	PF3D7_1011400	proteasome subunit β5
1E9 F9	Pf3D7_10_v3	441641	C	T	M45I	atG/atA	PF3D7_1011400	proteasome subunit β5
1E9 D11	Pf3D7_10_v3	441641	C	T	M45I	atG/atA	PF3D7_1011400	proteasome subunit β5

[a]The amino acid change is for the mature protein. The corresponding mutation in the full-length non-processed protein is M105I.

Table S8. Rat PK data for selected compounds

Compound	ROA[a]	AUC (24hr) (nM*hr)	t_{max} (h)	C_{max}[b] (nM)	$t_{1/2}$ (h)	C_L (L/hr/kg)	V_{ss} (L/kg)	%F
MPI-5	IV	1700	0.08	2670	4.4	1.2	2.1	--
	PO	853	0.3	505	4.0	--	--	50
MPI-10	IV	1440	0.08	1710	5.3	1.4	4.2	--
	PO	835	0.5	282	4.8	--	--	58
MPI-11	IV	2340	0.08	4120	5.3	0.82	1.3	--
	PO	2660	0.3	1400	3.7	--	--	113
MPI-13	IV	2070	0.08	2660	5.3	0.87	2.3	--
	PO	1640	0.5	666	3.2	--	--	78

[a]All compounds were dosed at 1 mg/kg IV and PO and all data is based on plasma levels of compound.

[b]For IV, C_{max} is the concentration at 5 min post dose (maximum sampled concentration).

Table S9. SCID mouse PK data for efficacy studies

Compound	Dose (PO, mg/kg)	Mean blood concentrations (ng/mL) in SCID mice				
		Time (h)	n	Mean (ng/mL)	SD (ng/mL)	CV (%)
MPI-5	50	1.0	2	1630	240	15
		2.0	2	730	120	17
		4.0	2	440	69	16
		6.0	2	240	20	8
		24	2	0	0	
MPI-13	25	1	2	240	14	6
		2	2	89	0.8	1
		4	2	18	0.8	4
		6	2	15	2	11
		24	2	< 10.0		

Table S10. Cryo-EM data collection and model building

	*Pf*20S/bortezomib	*Pf*20S/MPI-5	*Hs*20S/MPI-5
Data collection and image processing			
Magnification	100,000		
Electron energy (kV)	200		
Electron exposure ($e^-/Å^2$)	50		
Defocus range (μm)	0.4-1.6	0.5-1.5	0.6-1.6
Pixel size (Å)	1.31		
Starting model	*De novo*		
Symmetry imposed	C2		
Total number of micrographs	2430	1498	1551
Initial particle images	88785	73933	338438
Final particle images	24536	38738	192367
Map resolution (Å)	3.4	3.1	3.4
FSC threshold	0.143		
EMDB code	EMD-23574	EMD-23575	EMD-23576

| Model building and refinement			
Initial models used	PDB 6MUV [9]	PDB 6MUV [10]	PDB 5LF3 [11]
Model resolution (Å)	3.6	3.3	3.6
FSC threshold	0.5		
Sharpening B factor (Å^2)	73	64	129
Model composition			
Non-hydrogen atoms	50536	50778	48314
Amino acid residues	6318	6364	6204
Protein molecules	28	28	28
Ligands	6	2	2
Real-space correlation			
CCvolume	0.81	0.82	0.80
CCmask	0.82	0.83	0.80
Mean protein B factors (Å^2)	75.71	65.51	80.40
Mean ligand B factors (Å^2)	61.80	68.27	74.86
RMS deviations			
Bond lengths (Å) (outliers > 4σ)	0.009 (0)	0.006 (0)	0.006 (0)
Bond angles (°) (outliers > 4σ)	0.833 (12)	0.676 (14)	0.878 (28)
Validation			
MolProbity score [c]	2.31	2.14	1.53
Clashscore	17.54	14.15	8.89
Rotamer outliers (%)	0.79	0.46	0.16
CaBLAM outliers (%) [i]	4.69	4.14	1.22
Cβ outliers	0	0	0
Ramachandran plot			
Favored (%)	89.26	92.17	97.75
Allowed (%)	10.70	7.83	1.92
Outliers (%)	0.03	0.00	0.33
PDB code	7LXT	7LXU	7LXV

Supplementary Methods

Chemical synthesis and characterization

Aminoboronate synthesis

To prepare the compounds in this manuscript, four different aminoboronates were required. Three were prepared as described below from the corresponding aryl bromides which were either commercially available or prepared as described below, and one aminoboronate ((R)-2-phenyl-1-((3aS,4S,6S,7aR)-3a,5,5-trimethylhexahydro-4,6-methanobenzo[d][1,3,2]dioxaborol-2-yl)ethan-1-amine) is commercially available.

Boronate 1
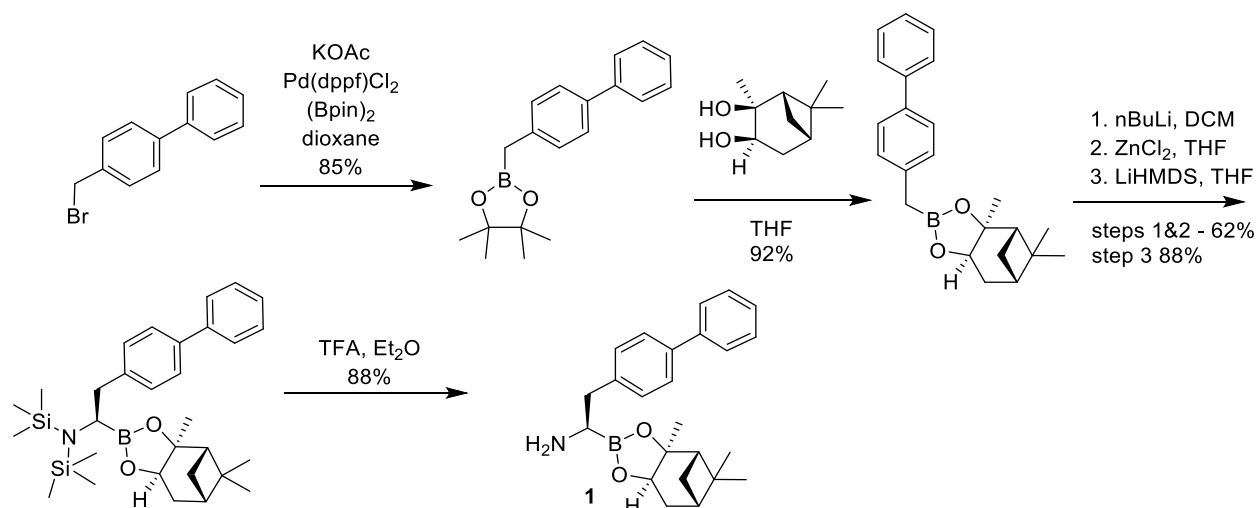
Scheme S1.

1-1.　A solution of 4-(bromomethyl)-1,1'-biphenyl (84 g, 339 mmol), 4,4,5,5-tetramethyl-2-(4,4,5,5-tetramethyl-1,3,2-dioxaborolan-2-yl)-1,3,2-dioxaborolane (103 g, 406 mmol), Pd(dppf)Cl$_2$ (13.2g, 16.9 mmol, dichloromethane complex) and potassium acetate (99.1 g, 1010 mmol) in 1, 4-dioxane (1.5 L) was heated to 100°C for 6 h. The reaction mixture was filtered through Celite®, the filtrate was concentrated in vacuo and the residue was purified by column chromatography (SiO$_2$, elution with 0-7% ethyl acetate in petroleum ether) to provide 2-([1,1'-biphenyl]-4-ylmethyl)-4,4,5,5-tetramethyl-1,3,2-dioxaborolane (85 g, 85% yield) as a yellow solid. ^{1}H NMR (400 MHz, CDCl$_3$) δ 7.56 - 7.63 (m, 2 H), 7.40 - 7.53 (m, 4 H), 7.26 - 7.36 (m, 3 H), 2.36 (s, 2 H), 1.27 (s, 12 H).

1-2.　A mixture of 2-([1,1'-biphenyl]-4-ylmethyl)-4,4,5,5-tetramethyl-1,3,2-dioxaborolane (85 g, 288 mmol) and (1S,2S,3R,5S)-2,6,6-trimethylbicyclo[3.1.1]heptane-2,3-diol (83.2 g, 489 mmol) in THF (1 L) was heated at 75°C for 20 h. The reaction mixture was concentrated in vacuo, and the residue was purified by column chromatography (SiO$_2$, elution with 0-5% ethyl acetate in petroleum ether) to give (3aS,4S,6S,7aR)-2-([1,1'-biphenyl]-4-ylmethyl)-3a,5,5-trimethylhexahydro-4,6-methanobenzo[d][1,3,2]dioxaborole (84 g, 92% yield) as a white solid. ^{1}H NMR (400 MHz, CDCl$_3$) δ 7.51 - 7.58 (m, 2 H), 7.45 (d, *J*=8.0 Hz, 2 H), 7.33 - 7.41 (m, 2 H), 7.22 - 7.31 (m, 3 H), 4.26 (dd, *J*=8.8, 2.0 Hz, 1 H), 2.24 - 2.38 (m, 3 H), 2.16 (dtd, *J*=10.8, 6.2, 6.2, 2.1 Hz, 1 H), 2.01 (m. 1 H), 1.76 - 1.90 (m, 2 H), 1.35 - 1.39 (m, 3 H), 1.24 (s, 4 H), 1.06 (d, *J*=10.8 Hz, 1 H), 0.80 (s, 3 H).

1-3.　To a solution of dichloromethane (18.5 mL, 290 mmol) and THF (800 mL) at -90°C, was added a solution of *n*-BuLi (101 mL, 254 mmol, 1.9 M in THF) and the resulting mixture was stirred at -90°C for 20 min. A solution of (3aS,4S,6S,7aR)-2-([1,1'-biphenyl]-4-ylmethyl)-3a,5,5-trimethylhexahydro-4,6-methanobenzo[d][1,3,2]dioxaborole (84 g, 242 mmol) in THF (200 mL) was added to the cooled mixture in one portion, and the reaction mixture temperature

rose to -70°C. The mixture was stirred at -80 to -85°C for 20 min and then a solution of ZnCl$_2$ (133 mL, 254 mmol, 1.9 M in THF) was added. The resulting mixture was warmed to 20°C and stirred for 1 h. The reaction mixture was then treated with saturated NH$_4$Cl solution (800 mL) and extracted with petroleum ether (500 mL). The organic phase was isolated, dried over Na$_2$SO$_4$, filtered and concentrated. The residue was purified by column chromatography (SiO$_2$, elution with 2-5% ethyl acetate in petroleum ether) and the resulting material was triturated with petroleum ether (30 mL) at 0°C to give (3aS,4S,6S,7aR)-2-(2-([1,1'-biphenyl]-4-yl)-1-chloroethyl)-3a,5,5-trimethylhexahydro-4,6-methanobenzo[d][1,3,2]dioxaborole (59 g, 62% yield). ^{1}H NMR (400 MHz, DMSO-d_6) δ 7.63 - 7.68 (m, 2 H), 7.60 (d, J=8.2 Hz, 2 H), 7.46 (t, J=7.6 Hz, 2 H), 7.33 - 7.40 (m, 3 H), 4.44 (dd, J=8.7, 1.7 Hz, 1 H), 3.86 (dd, J=8.9, 7.0 Hz, 1 H), 3.21 (dd, J=14.0, 6.9 Hz, 1 H), 2.95 - 3.10 (m, 1 H), 2.28 - 2.38 (m, 1 H), 2.10 - 2.22 (m, 1 H), 1.82 - 1.90 (m, 1 H), 1.68 - 1.77 (m, 1 H), 1.20 - 1.33 (m, 7 H), 1.01 (d, J=10.9 Hz, 1 H), 0.78 - 0.83 (m, 3 H).

1-4. A solution of (3aS,4S,6S,7aR)-2-(2-([1,1'-biphenyl]-4-yl)-1-chloroethyl)-3a,5,5-trimethylhexahydro-4,6-methanobenzo[d][1,3,2]dioxaborole (59 g, 149 mmol) in THF (1 L) at -65°C was treated with a solution of LiHMDS (156 mL, 156 mmol, 1 M in THF). The resulting mixture was stirred at -65°C for 20 min and then warmed to 20 °C and stirred for 1 h. The reaction mixture was concentrated, and the residue was dissolved in petroleum ether (100 mL), cooled to 0°C, and filtered. The filtrate was concentrated to give N-((R)-2-([1,1'-biphenyl]-4-yl)-1-((3aS,4S,6S,7aR)-3a,5,5-trimethylhexahydro-4,6-methanobenzo[d][1,3,2]dioxaborol-2-yl)ethyl)-1,1,1-trimethyl-N-(trimethylsilyl)silanamine (68 g, 88% yield) as a pale yellow oil. ^{1}H NMR (400 MHz, CDCl$_3$) δ 7.56 - 7.61 (m, 2 H), 7.48 (d, J=8.1 Hz, 2 H), 7.39 - 7.45 (m, 2 H), 7.29 - 7.35 (m, 3 H), 4.28 (dd, J=8.7, 1.7 Hz, 1 H), 3.07 (dd, J=13.0, 7.5 Hz, 1 H), 2.85 (t, J=7.5 Hz, 1 H), 2.69 (dd, J=13.1, 7.5 Hz, 1 H), 2.22 - 2.35 (m, 1 H), 2.06 - 2.16 (m, 1 H), 2.00 (t, J=5.6 Hz, 1 H), 1.72 - 1.89 (m, 2 H), 1.37 (s, 3 H), 1.22 - 1.29 (m, 4 H), 0.95 (d, J=10.8 Hz, 1 H), 0.82 (s, 3 H), 0.09 (s, 17 H).

1-5. To a cooled solution of N-((R)-2-([1,1'-biphenyl]-4-yl)-1-((3aS,4S,6S,7aR)-3a,5,5-trimethylhexahydro-4,6-methanobenzo[d][1,3,2]dioxaborol-2-yl)ethyl)-1,1,1-trimethyl-N-(trimethylsilyl)silanamine (68 g, 130 mmol) in diethyl ether (600 mL) at -60 °C was added TFA (44.4 g, 390 mmol). The resulting reaction mixture was warmed to 20°C and stirred for 1 h. A white solid formed and the mixture was diluted with petroleum ether (600 mL) and stirred for 20 min. The solid was collected by filtration and dried in vacuo to give (R)-2-([1,1'-biphenyl]-4-yl)-1-((3aS,4S,6S,7aR)-3a,5,5-trimethylhexahydro-4,6-methanobenzo[d][1,3,2]dioxaborol-2-yl)ethan-1-amine (**1**, 56 g, 88% yield) as a white solid. ^{1}H NMR (400 MHz, CDCl$_3$) δ 7.88 (br s, 2 H), 7.53 (dd, J=13.1, 7.8 Hz, 4 H), 7.42 (t, J=7.5 Hz, 2 H), 7.31 - 7.37 (m, 3 H), 4.30 (br d, J=7.5 Hz, 1 H), 3.04 - 3.27 (m, 3 H), 2.09 - 2.27 (m, 2 H), 1.95 (t, J=5.3 Hz, 1 H), 1.77 - 1.89 (m, 2 H), 1.32 (s, 3 H), 1.22 (s, 3 H), 1.01 (d, J=11.3 Hz, 1 H), 0.75 (s, 3 H). $[\alpha]^{20}_D$ = -4° (c 1.00, methanol).

*Boronate **2***
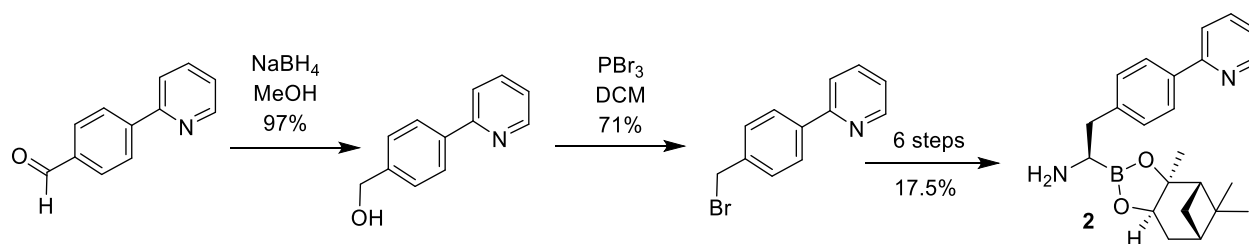
Scheme S2.

1-6.   To a 0°C solution of 4-(pyridin-2-yl)benzaldehyde (7.65 g, 41.7 mmol) in ethanol (120 mL) was added NaBH₄ (2.36 g, 62.5 mmol). The reaction mixture was stirred at 20°C for 4 h and then concentrated in vacuo. The residue was dissolved in ethyl acetate (100 mL) and water (80 mL), the phases were separated, and the aqueous phase was washed with ethyl acetate (100 mL twice). The combined organic phases was concentrated to give [4-(pyridin-2-yl)phenyl]methanol (7.5 g, 97% yield). ¹H NMR (400 MHz, CDCl₃) δ 8.70 (br d, *J*=3.8 Hz, 1 H), 7.97 (br d, *J*=8.0 Hz, 2 H), 7.75 (m, 2 H), 7.46 (br d, *J*=7.8 Hz, 2 H), 7.26 (m, 1 H), 4.76 (br s, 2 H).

1-7.   To a 0°C solution of [4-(pyridin-2-yl)phenyl]methanol (1.5 g 8.09 mmol) in dichloromethane (30 mL) was added PBr₃ (2.4g, 8.89 mmol). The resulting mixture was warmed to 20°C and stirred for 1 h. The reaction mixture was then poured into cold water (80 mL) and the pH of the resulting mixture was adjusted to around 8 by the addition of solid NaHCO₃. The phases were separated, and the aqueous phase was extracted with dichloromethane (80 mL) twice. The combined organic phases were washed with brine (80 mL), dried over Na₂SO₄, filtered and concentrated to give 2-[4-(bromomethyl)phenyl]pyridine (7.9 g, 71% yield). ¹H NMR (400 MHz, CDCl₃) δ 8.72 (m, 1 H), 8.00 (m, 2 H), 7.77 (m, 2 H), 7.53 (m, 2 H), 7.26 (m, 1 H), 4.58 (s, 2 H).

1-8.   2-4-(bromomethyl)phenyl]pyridine was taken through steps 1-5 above to provide (R)-2-(4-(pyridin-2-yl)phenyl)-1-((3aS,4S,6S,7aR)-3a,5,5-trimethylhexahydro-4,6-methanobenzo[d][1,3,2]dioxaborol-2-yl)ethan-1-amine as the trifluoroacetic acid salt, a pink solid (**2**, 17.5% overall yield). ¹H NMR (400 MHz, CDCl₃) δ 8.90 (d, *J*=4.8 Hz, 1 H), 8.19 (m, 1 H), 7.94 (br d, *J*=8.0 Hz, 3 H), 7.80 (d, *J*=8.3 Hz, 2 H), 7.61 (m, 1 H), 7.46 (d, *J*=8.3 Hz, 2 H), 4.38 (d, *J*=7.5 Hz, 1 H), 3.28 (br d, *J*=5.8 Hz, 1 H), 3.18 (m, 1 H), 3.09 (m, 1 H), 2.30 (m, 1 H), 2.22 (m, 1 H), 2.02 (m, 1 H), 1.89 (m, 2 H), 1.39 (s, 3 H), 1.28 (s, 4 H), 1.10 (d, *J*=11.0 Hz, 1 H), 0.87 (m, 1 H), 0.82 (s, 3 H). $[\alpha]^{19.5}_D$ = +3.8° (c 1.00, methanol)

*Boronate **3***
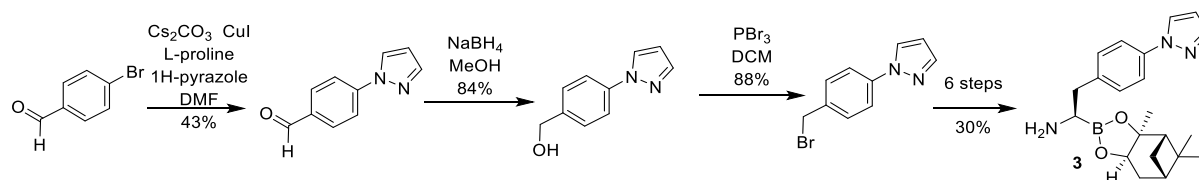
Scheme S3.

1-9.   To a solution of 4-bromobenzaldehyde (2.00 g, 10.8 mmol) in DMF (20 mL) at room temperature was added pyrazole (668 mg, 9.82 mmol), CuI (185 mg, 972 mmol), L-proline (223 mg, 1.94 mmol) and Cs₂CO₃ (6.40 g, 19.7 mmol). The reaction mixture was heated at 120°C for 20 h, cooled to room temperature and filtered. The filtrate was concentrated, and the residue was purified by column chromatography (SiO₂, elution with 10-20% ethyl acetate in petroleum ether) to provide 4-(1H-pyrazol-1-yl)benzaldehyde (12.0 g, 43% yield) as a pale yellow solid. ¹H NMR (400 MHz, DMSO-d₆) 9.96 - 10.05 (m, 1 H), 8.68 (d, *J*=2.6 Hz, 1 H), 8.00 - 8.14 (m, 4 H), 7.85 (d, *J*=1.3 Hz, 1 H), 6.63 (dd, *J*=2.6, 1.8 Hz, 1 H), 6.59 - 6.66 (m, 1 H).

1-10.   1-[4-(bromomethyl)phenyl]-1H-pyrazole was prepared from 4-(1H-pyrazol-1-yl)benzaldehyde under the conditions described in steps 6 and 7 above in 74% yield. ¹H NMR (400 MHz, CDCl₃) δ 7.93 (d, *J*=2.6 Hz, 1 H), 7.64 - 7.80 (m, 3 H), 7.49 (d, *J*=8.3 Hz, 2 H), 6.48 (t, *J*=2.2 Hz, 1 H), 4.54 (s, 2 H).

1-11.   1-[4-(bromomethyl)phenyl]-1H-pyrazole was taken through steps 1-4 above to provide [(1R)-2-[4-(1H-pyrazol-1-yl)phenyl]-1-[(1S,2S,6R,8S)-2,9,9-trimethyl-3,5-dioxa-4-boratricyclo[6.1.1.0^{2,6}]decan-4-yl]ethyl]bis(trimethylsilyl)amine as a pale yellow solid (34% yield through 4 steps).

1-12.   A -65°C solution of [(1R)-2-[4-(1H-pyrazol-1-yl)phenyl]-1-[(1S,2S,6R,8S)-2,9,9-trimethyl-3,5-dioxa-4-boratricyclo[6.1.1.0^{2,6}]decan-4-yl]ethyl]bis(trimethylsilyl)amine (8.7 g, 17.0 mmol) in diethyl ether (50 mL) was treated with a solution of HCl (17.0 mL, 51 mmol, 3.0 M in Et$_2$O). The reaction mixture was stirred for 10 min and a solid precipitate formed. Petroleum ether (30 mL) was added and the reaction mixture was warmed to room temperature, stirred for 30 min and filtered. The solid was dried under vacuum to give (1R)-2-[4-(1H-pyrazol-1-yl)phenyl]-1-[(1S,2S,6R,8S)-2,9,9-trimethyl-3,5-dioxa-4-boratricyclo[6.1.1.0^{2,6}]decan-4-yl]ethan-1-amine hydrochloride (**3**, 7.2 g, 89% yield) as a pale yellow solid. ^{1}H NMR (400 MHz, CDCl$_3$) δ 8.20 (br s, 3 H), 7.99 (br s, 1 H), 7.80 (s, 1 H), 7.64 (br d, J=7.9 Hz, 2 H), 7.51 (br d, J=7.9 Hz, 2 H), 6.51 (s, 1 H), 4.37 (br d, J=7.9 Hz, 1 H), 3.72 (br s, 4 H), 3.16 - 3.37 (m, 3 H), 2.10 - 2.34 (m, 2 H), 1.98 (br t, J=5.3 Hz, 1 H), 1.81 - 1.94 (m, 2 H), 1.37 (s, 3 H), 1.23 (s, 3 H), 1.09 - 1.17 (m, 1 H), 0.77 (s, 3 H). [α]$^{25}_D$ = +2° (c 1.00, methanol).
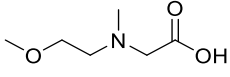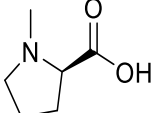
Synthesis of MPI-10

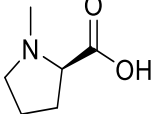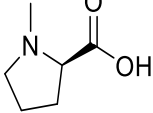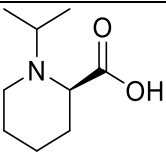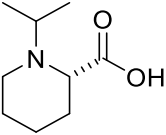MPI-10
pinane ester

MPI-10
citrate ester
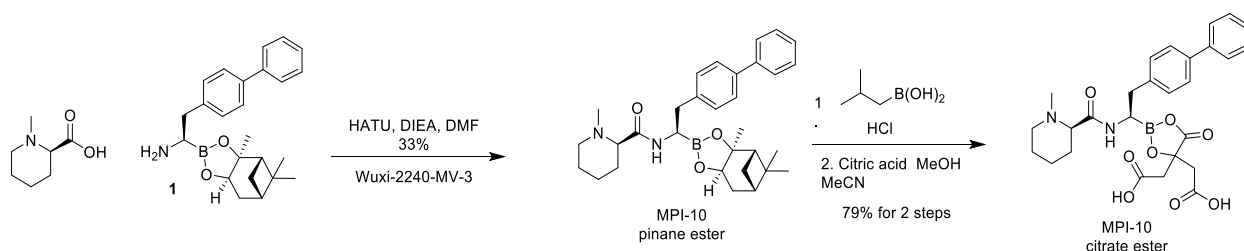
Scheme S4.

2-1.   To a solution of (R)-2-([1,1'-biphenyl]-4-yl)-1-((3aS,4S,6S,7aR)-3a,5,5-trimethylhexahydro-4,6-methanobenzo[d][1,3,2]dioxaborol-2-yl)ethan-1-amine (600 mg, 1.22 mmol), (2R)-1-methylpiperidine-2-carboxylic acid (209 mg, 1.46 mmol) in DMF (6 mL) was added DIPEA (0.657 mL, 473 mg, 3.66 mmol) and 1-[bis(dimethylamino)methylene]-1H-1,2,3-triazolo[4,5-b]pyridinium 3-oxide hexafluorophosphate, (HATU, 555 mg, 1.46 mmol). The resulting mixture was stirred for 2 h at 20°C. Water (10 mL) was added and a yellow precipitate formed. The solid was collected by filtration, washed with acetonitrile (10 mL) and dried under vacuum to give (R)-N-((R)-2-([1,1'-biphenyl]-4-yl)-1-((3aS,4S,6S,7aR)-3a,5,5-trimethylhexahydro-4,6-methanobenzo[d][1,3,2]dioxaborol-2-yl)ethyl)-1-methylpiperidine-2-carboxamide (210 mg, 33% yield) as a white solid. ^{1}H NMR (400 MHz, CDCl$_3$) δ 7.52 (d, J=7.4 Hz, 2 H), 7.47 (d, J=8.0 Hz, 2 H), 7.37 (t, J=7.6 Hz, 2 H), 7.27 (m, 1 H), 7.21 (d, J=8.1 Hz, 2 H), 6.74 (br s, 1 H), 4.23 (m, 1 H), 3.03 (m, 1 H), 2.95 (m, 1 H), 2.76 (m, 2 H), 2.51 (dd, J=11.0, 3.0 Hz, 1 H), 2.26 (m, 1 H), 2.04 (m, 4 H), 1.93 (m, 3 H), 1.79 (m, 2 H), 1.67 (br d, J=12.8 Hz, 1 H), 1.48 (m, 1 H), 1.34 (m, 5 H), 1.29 (br d, J=10.4 Hz, 1 H), 1.21 (s, 3 H), 1.14 (m, 1 H), 0.79 (s, 3 H). HRMS (ESI): *m/z* calculated for the boronic acid C$_{21}$H$_{27}$BN$_2$O$_3$ + H$^+$ [M + H$^+$]: 367.2193. Found: 367.2195.
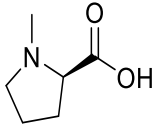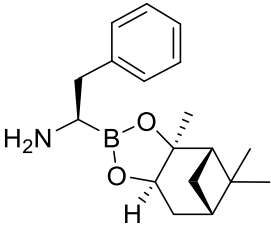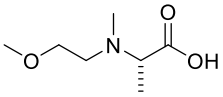
2-2.   To a suspension of (R)-N-((R)-2-([1,1'-biphenyl]-4-yl)-1-((3aS,4S,6S,7aR)-3a,5,5-trimethylhexahydro-4,6-methanobenzo[d][1,3,2]dioxaborol-2-yl)ethyl)-1-methylpiperidine-2-carboxamide (65 mg, 0.130 mmol) in hexane (3 mL) was added isobutylboronic acid (41.8 mg, 0.390 mmol) and a solution of HCl (1 mL, 1 mmol, 1 M) followed by methanol (2 mL) and the reaction mixture was stirred for 1 h. The reaction mixture was diluted with methanol and the methanol solution was washed with hexane three times and then concentrated in vacuo. The resulting residue was

dissolved in acetonitrile, filtered, concentrated in vacuo and dried under vacuum to give the HCl salt of [(1R)-1-[[(2R)-1-methylpiperidine-2-carbonyl]amino]-2-(4-phenylphenyl)ethyl]boronic acid (44 mg, 84%) as an off-white solid. This material was used without further purification in the next step.

2-3. The hydrochloride salt of [(1R)-1-[[(2R)-1-methylpiperidine-2-carbonyl]amino]-2-(4-phenylphenyl)ethyl]boronic acid (43 mg, 0.1068 mmol) was dissolved in methanol (1 mL) and acetonitrile (5 mL). To the solution was added dropwise a solution of citric acid (20.5 mg, 0.107 mmol) in acetonitrile (approximately 2 mL) and the resulting mixture was stirred for 2 h at 60ºC, cooled to room temperature and concentrated in vacuo. The residue was suspended in ethyl acetate and the mixture was sonicated for a while. The solution was decanted, and this process was repeated twice. The resulting residue was dissolved in acetonitrile and filtered. The filtrate was concentrated in vacuo and the residue was dried to give the desired product (57 mg, 94%) as an off-white solid. ^{1}H NMR (400 MHz, CD$_3$OD) δ 1.53 - 1.65 (m, 1 H), 1.66 - 1.84 (m, 2 H), 1.85 - 2.04 (m, 3 H), 2.73 - 3.00 (m, 8 H), 3.04 - 3.17 (m, 1 H), 3.35 - 3.44 (m, 1 H), 3.47 (br s, 1 H), 3.49 - 3.59 (m, 1 H), 3.63 - 4.06 (m, 1 H), 3.63 - 3.73 (m, 1 H), 7.30 - 7.36 (m, 2 H), 7.36 - 7.47 (m, 3 H),7.53 - 7.62 (m, 4 H).

The compounds listed below were prepared as described above using the amines and aminoboronates listed in steps 2-1 to 2-3.

Compound	Yield for Step 2-1	Amine for Step 2-1	Aminoboronate for Step 2-1	Yield for Steps 2-2 and 2-3
MPI-11	55%		1	94%
MPI-5	62%		1	NA
MPI-8	18%		2	NA
MPI-9	25%		3	NA
MPI-13	37%		1	NA
MPI-14	36%		1	NA

MPI-7	62%			NA
MPI-12	11%		**1**	88%

Compound	Pinane ester ^{1}H NMR and HRMS Data	Citrate ester ^{1}H NMR and HRMS Data
MPI-11	^{1}H NMR (400 MHz, CDCl$_3$) δ 8.05 (br s, 1 H), 7.57 (m, 4 H), 7.45 (t, J=7.6 Hz, 2 H), 7.34 (m, 3 H), 4.27 (dd, J=8.6, 2.0 Hz, 1 H), 3.29 (m, 4 H), 3.06 (m, 5 H), 2.83 (m, 1 H), 2.55 (m, 2 H), 2.33 (m, 4 H), 2.13 (m, 1 H), 2.03 (t, J=5.4 Hz, 1 H), 1.88 (m, 2 H), 1.42 (s, 3 H), 1.38 (d, J=10.4 Hz, 1 H), 1.29 (s, 3 H), 0.88 (s, 3 H). HRMS (ESI): *m/z* calculated for the boronic acid C$_{20}$H$_{27}$BN$_2$O$_4$ + H$^+$ [M + H$^+$]: 371.2142. Found: 371.2147.	^{1}H NMR (400 MHz, CD$_3$OD) δ 7.54 - 7.65 (m, 4 H), 7.44 (td, J=7.67, 1.90 Hz, 2 H), 7.31 - 7.40 (m, 3 H), 4.05 - 4.30 (m, 1 H), 3.95 (br s, 1 H), 3.57 - 3.70 (m, 2 H), 3.35 - 3.53 (m, 4 H), 2.78 - 3.05 (m, 8 H). HRMS (ESI): *m/z* calculated for the boronic acid C$_{20}$H$_{27}$BN$_2$O$_4$ + H$^+$ [M + H$^+$]: 371.2142. Found: 371.2142.
MPI-5	^{1}H NMR (400 MHz, CDCl$_3$) δ 7.52 (br d, J=7.6 Hz, 2 H), 7.47 (br d, J=8.0 Hz, 2 H), 7.37 (m, 3 H), 7.27 (m, 1 H), 7.21 (s, 2 H), 4.21 (br d, J=7.1 Hz, 1 H), 2.97 (m, 4 H), 2.71 (m, 1 H), 2.25 (m, 2 H), 2.19 (s, 3 H), 2.14 (m, 1 H), 2.06 (m, 1 H), 1.94 (br t, J=5.3 Hz, 1 H), 1.81 (m, 3 H), 1.69 (m, 1 H), 1.62 (m, 1 H), 1.33 (m, 4 H), 1.20 (m, 4 H), 0.79 (s, 3 H). HRMS (ESI): *m/z* calculated for the boronic acid C$_{20}$H$_{25}$BN$_2$O$_3$ + H$^+$ [M + H$^+$]: 353.2036. Found: 353.2040.	^{1}H NMR (400 MHz, CD$_3$CN) δ 8.03 - 11.79 (m, 2 H), 7.59 - 7.69 (m, 4 H), 7.48 (t, J=7.64 Hz, 2 H), 7.34 - 7.44 (m, 3 H), 4.10 - 4.29 (m, 1 H), 3.76 - 3.95 (m, 1 H), 3.20 - 3.39 (m, 1 H), 2.46 (br d, J=7.95 Hz, 1 H), 3.06 (br dd, J=14.37, 3.48 Hz, 2 H), 2.60 - 2.88 (m, 8 H). HRMS (ESI): *m/z* calculated for the boronic acid C$_{20}$H$_{25}$BN$_2$O$_3$ + H$^+$ [M + H$^+$]: 353.2036. Found: 353.2038.
MPI-8	^{1}H NMR (400 MHz, CDCl$_3$) δ 8.69 (d, J=4.3 Hz, 1 H), 7.93 (d, J=8.3 Hz, 2 H), 7.74 (m, 2 H), 7.46 (br s, 1 H), 7.31 (d, J=8.3 Hz, 2 H), 7.23 (ddd, J=6.8, 5.0, 1.5 Hz, 1 H), 4.29 (m, 1 H), 3.04 (m, 3 H), 2.77 (m, 1 H), 2.33 (m, 2 H), 2.24 (s, 3 H), 2.16 (m, 1 H), 2.03 (m, 1 H), 1.87 (m, 3 H), 1.77 (br s, 1 H), 1.62 (br s, 3 H), 1.41 (m, 4 H), 1.28 (s, 3 H), 0.87 (s, 3 H). HRMS (ESI):	NA

|		
	m/z calculated $C_{29}H_{38}BN_3O_2$ + H$^+$ [M + H$^+$]: 488.308447. Found: 488.3096.	
MPI-9	^{1}H NMR (400 MHz, CDCl$_3$) δ 7.83 (d, J=2.5 Hz, 1 H), 7.65 (d, J=1.6 Hz, 1 H), 7.55 (d, J=8.4 Hz, 2 H), 7.36 (br s, 1 H), 7.21 (d, J=8.4 Hz, 2 H), 6.40 (t, J=2.0 Hz, 1 H), 4.21 (m, 1 H), 2.95 (m, 4 H), 2.69 (m, 1 H), 2.24 (m, 2 H), 2.19 (s, 3 H), 2.10 (m, 2 H), 1.95 (t, J=5.4 Hz, 1 H), 1.80 (m, 3 H), 1.71 (m, 1 H), 1.60 (m, 1 H), 1.33 (m, 4 H), 1.21 (s, 3 H), 0.79 (s, 3 H). HRMS (ESI): m/z calculated for the boronic acid $C_{17}H_{23}BN_4O_3$ + H$^+$ [M + H$^+$]: 343.1941. Found: 343.1935.	NA
MPI-14	^{1}H NMR (500 MHz, CDCl$_3$) δ 7.51 - 7.61 (m, 4 H), 7.44 (t, J = 7.6 Hz, 2 H), 7.27 – 7.37 (m, 3H), 6.92 (br s, 1 H), 4.24 – 4.35 (m, 3 H), 2.65 – 2.86 (m, 3 H), 2.28 – 2.40 (m, 1 H), 2.08 – 2.25 (m, 2 H), 1.98 – 2.05 (m, 3 H), 1.47 – 1.71 (m, 10 H), 0.79 – 0.91 (m, 9 H). HRMS (ESI): m/z calculated for the boronic acid $C_{23}H_{31}BN_2O_3$ + H$^+$ [M + H$^+$]: 395.250597. Found: 395.2510.	NA
MPI-13	^{1}H NMR (500 MHz, CDCl$_3$) δ 7.52 - 7.62 (m, 4 H), 7.45 (t, J=7.7 Hz, 2 H), 7.32 - 7.38 (m, 1 H), 7.30 (d, J=8.1 Hz, 2 H), 6.93 (br s, 1 H), 4.31 (dd, J=8.6, 1.8 Hz, 1 H) 4.13 (q, J=7.2 Hz, 1 H), 3.09 - 3.20 (m, 2 H), 3.05 (dd, J=14.3, 4.6 Hz, 1 H), 2.68 - 2.86 (m, 3 H), 2.31 - 2.39 (m, 1 H), 2.11 - 2.25 (m, 2 H), 2.00 - 2.05 (m, 1 H), 1.84 - 1.97 (m, 3 H), 1.48 - 1.73 (m, 5 H), 1.40 - 1.45 (m, 3 H), 1.34 - 1.39 (m, 2 H), 1.29 (s, 3 H), 0.79 - 0.95 (m, 9 H). HRMS (ESI): m/z calculated for the boronic acid $C_{23}H_{31}BN_2O_3$ + H$^+$ [M + H$^+$]: 395.250597. Found: 395.2513.	^{1}H NMR (400 MHz, DMSO-$d6$) δ 12.10 (br s, 1 H), 9.11 (br s, 1 H), 7.90 - 8.35 (m, 1 H), 7.61 (br s, 2 H), 7.38 - 7.55 (m, 4 H), 7.18 - 7.37 (m, 3 H), 3.74 (br s, 1 H), 3.49 - 3.61 (m, 2 H), 2.82 (br s, 2 H), 2.72 (br s, 1 H), 2.57 (br s, 2 H), 2.39 (br d, J=16.51 Hz, 1 H), 1.69 (br s, 3 H), 1.55 (br s, 1 H), 1.26 - 1.38 (m, 1 H), 1.20 (br s, 3 H), 1.10 (br s, 3 H).
MPI-7	^{1}H NMR (400 MHz, CDCl$_3$) δ 7.43 (br s, 1 H), 7.28 - 7.35 (m, 2 H), 7.16 - 7.25 (m, 3 H), 4.21 - 4.33 (m, 1 H), 2.93 - 3.10 (m, 4 H), 2.65 - 2.79 (m, 1 H), 2.27 - 2.39 (m, 2 H), 2.25 (s, 3 H), 2.08	NA

	- 2.22 (m, 2 H), 2.01 (t, *J*=5.5 Hz, 1 H), 1.82 - 1.95 (m, 3 H), 1.73 - 1.81 (m, 1 H), 1.67 - 1.72 (m, 1 H), 1.67 - 1.72 (m, 1 H), 1.41 (s, 3 H), 1.37 (d, *J*=10.5 Hz, 1 H), 1.23 - 1.32 (m, 3 H), 0.87 (s, 3 H). HRMS (ESI): *m/z* $C_{24}H_{35}BN_2O_3$ + H$^+$ [M + H$^+$]: 411.281898. Found: 411.2829.	
MPI-12	^{1}H NMR (400 MHz, CDCl$_3$) δ 8.45 (br s, 1 H), 7.55 (dd, *J*=13.2, 7.7 Hz, 4 H), 7.43 (t, *J*=7.7 Hz, 2 H), 7.29 - 7.37 (m, 3 H), 4.23 (br d, *J*=7.0 Hz, 1 H), 3.50 (q, *J*=6.6 Hz, 1 H), 3.25 - 3.34 (m, 1 H), 3.15 - 3.22 (m, 1 H), 2.97 - 3.08 (m, 2 H), 2.87 (s, 3 H), 2.69 - 2.79 (m, 1 H), 2.47 - 2.59 (m, 1 H), 2.23 - 2.38 (m, 5 H), 2.06 - 2.14 (m, 1 H), 2.00 (t, *J*=5.4 Hz, 1 H), 1.81 - 1.89 (m, 2 H), 1.60 (s, 1 H), 1.36 - 1.47 (m, 4 H), 1.20 - 1.30 (m, 6 H), 0.87 (s, 3 H).	^{1}H NMR (400 MHz, CD$_3$OD) δ 7.52 - 7.65 (m, 4 H), 7.33 - 7.48 (m, 5 H), 3.87 - 4.08 (m,1 H), 3.49 (br d, *J*=19.81 Hz, 4 H), 3.25 (br s, 2 H), 2.60 - 3.15 (m, 11 H), 1.48 - 1.60 (m, 3 H). HRMS (ESI): *m/z* calculated for the boronic acid $C_{21}H_{29}BN_2O_4$ + H$^+$ [M + H$^+$]: 385.229863. Found: 385.2305.

Synthesis of (2R)-1-(propan-2-yl)piperidine-2-carboxylic acid

(2R)-piperidine-2-carboxylic acid (1.00 g, 7.74 mmol) was dissolved in dry methanol/acetone (2:1 mixture, 15 mL) and Pd(OH)$_2$ (294 mg, 387 mmol, 20% on carbon) was added and the resulting mixture was stirred under a hydrogen atmosphere (50 psi) for 24 h. The reaction mixture was filtered through Celite®, and the filtrate was concentrated in vacuo. The resulting pale yellow solid was triturated with ethyl acetate/methanol (10:1 mixture, 10 mL) and then dried to give (2R)-1-(propan-2-yl)piperidine-2-carboxylic acid (580 mg, 44% yield). ^{1}H NMR (400 MHz, CD$_3$OD) δ 3.86 (m, 1 H), 3.47 - 3.61 (m, 1 H), 3.27 (dt, *J*=3.1, 1.7 Hz, 1 H), 2.78 - 2.98 (m, 1 H), 2.10 - 2.27 (m, 1 H), 1.70 - 1.92 (m, 5 H), 1.45 - 1.67 (m, 2 H), 1.34 (d, *J*=6.8 Hz, 3 H), 1.23 (d, *J*=6.8 Hz, 3 H).

(2S)-1-(propan-2-yl)piperidine-2-carboxylic acid was prepared in 97% yield in a similar manner using (2S)-piperidine-2-carboxylic acid.

Synthesis of MPI-6
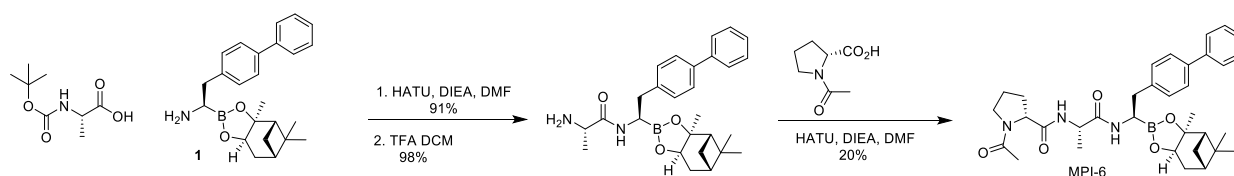
Scheme S5.

To a solution of 2S)-2-{[(tert-butoxy)carbonyl]amino}propanoic acid (230 mg, 1.22 mmol) in DMF (12 mL) at -40°C was added HATU (463 mg, 1.22 mmol) and (1R)-2-{[1,1'-biphenyl]-4-yl}-1-[(1S,2S,6R,8S)-2,9,9-trimethyl-3,5-dioxa-4-boratricyclo[6.1.1.0²,⁶]decan-4-yl]ethan-1-amine (500 mg, 1.02 mmol). DIPEA (0.732 mL, 527 mg, 4.08 mmol) was added and the mixture was stirred at -40°C for 10 min and at room temperature for 3 h. Water (30 mL) and ethyl acetate (30 mL) were added and the phases were separated. The aqueous phase was extracted twice with ethyl acetate (30 mL). The combined organic phases were washed twice with brine (20 mL), dried over Na2SO$_4$, filtered and concentrated to

give tert-butyl N-[(1S)-1-{[(1R)-2-{[1,1'-biphenyl]-4-yl}-1-[(1S,2S,6R,8S)-2,9,9-trimethyl-3,5-dioxa-4-boratricyclo[6.1.1.0²,⁶]decan-4-yl]ethyl]carbamoyl }ethyl]carbamate (580 mg, 99% yield) as a white solid. ¹H NMR (400 MHz, CDCl₃) δ 7.50 (d, J=7.25 Hz, 2 H), 7.44 (d, J=8.13 Hz, 2 H), 7.36 (t, J=7.63 Hz, 2 H), 7.27 (d, J=7.25 Hz, 1 H), 7.19 (t, J=4.00 Hz, 3 H), 6.49 (br s, 1 H), 4.80 (br s, 1 H), 4.21 - 4.30 (m, 1 H), 4.15 (br s, 1 H), 3.15 (br s, 1 H), 2.95 (br dd, J=14.20, 4.69 Hz, 1 H), 2.75 - 2.81 (m, 1 H), 2.20 - 2.32 (m, 1 H), 2.00 - 2.13 (m, 1 H), 1.91 - 1.98 (m, 1 H), 1.74 - 1.85 (m, 2 H), 1.26 - 1.36 (m, 15 H), 1.16 - 1.23 (m, 4 H), 0.78 (s, 3 H).

Tert-butylN-[(1S)-1-{[(1R)-2-{[1,1'-biphenyl]-4-yl}-1-[(1S,2S,6R,8S)-2,9,9-trimethyl-3,5-dioxa-4-boratricyclo[6.1.1.0²,⁶]decan-4-yl]ethyl]carbamoyl }ethyl]carbamate (100 mg, 0.146 mmol) in dicholormethane (2 mL) was treated with TFA (0.5 mL). The reaction mixture was stirred at room temperature for 2 h and then concentrated in vacuo. This provided (S)-N-((R)-2-([1,1'-biphenyl]-4-yl)-1-((3aS,4S,6S,7aR)-3a,5,5-trimethylhexahydro-4,6-methanobenzo[d][1,3,2]dioxaborol-2-yl)ethyl)-2-aminopropanamide as the TFA salt (80 mg, 98% yield).

(2R)-1-Acetylpyrrolidine-2-carboxylic acid (168 mg, 1.07 mmol) was dissolved in DMF (10 mL) and the solution was cooled to -40ºC. HATU (406 mg, 1.07 mmol) and ((S)-N-((R)-2-([1,1'-biphenyl]-4-yl)-1-((3aS,4S,6S,7aR)-3a,5,5-trimethylhexahydro-4,6-methanobenzo[d][1,3,2]dioxaborol-2-yl)ethyl)-2-aminopropanamide as the TFA salt (500 mg, 0.892 mmol) were added followed by DIPEA (0.653 mL, 460 mg, 3.56 mmol). The reaction mixture was stirred at -40ºC for 10 min and then at room temperature for 3 h. Water (20 mL) was added to the reaction mixture and a white solid precipitated. The solid was collected by filtration and the crude product was purified by HPLC (water (0.05% ammonia hydroxide v/v)-acetonitrile; Column: YMC Triart C18 250 x 50 mm x7 μm) to give (2S)-2-{[(2R)-1-acetylpyrrolidin-2-yl]formamido}-N-[(1R)-2-{[1,1'-biphenyl]-4-yl}-1-[(1S,2S,6R,8S)-2,9,9-trimethyl-3,5-dioxa-4-boratricyclo[6.1.1.0²,⁻0;]decan-4-yl]ethyl]propanamide (111 mg, 20% yield) as a white solid. ¹H NMR (400 MHz, CDCl₃) δ 9.43 (br s, 1 H), 9.04 (br s, 1 H), 7.24 - 7.57 (m, 9 H), 4.81 (br s, 1 H), 4.13 (br d, J=7.00 Hz, 1 H), 3.99 (br s, 1 H), 3.64 (br d, J=7.13 Hz, 1 H), 3.51 (br s, 1 H), 3.38 (br s, 1 H), 3.12 (br d, J=12.51 Hz, 1 H), 2.77 - 2.95 (m, 1 H), 2.06 - 2.24 (m, 5 H), 2.00 (br d, J=17.38 Hz, 2 H), 1.86 (br s, 3 H), 1.81 (br d, J=14.13 Hz, 2 H), 1.66 (br d, J=18.64 Hz, 2 H), 1.23 - 1.42 (m, 4 H), 1.16 (br s, 3 H), 0.81 (br s, 3 H), 0.49 (br d, J=8.25 Hz, 1 H). HRMS (ESI): m/z calculated $C_{34}H_{44}BN_3O_5 + H^+$ [M + H⁺]: 586.345227. Found: 586.3474.

Chemical and physicochemical characterization

High-resolution mass spectrometry (HRMS) analysis was performed using Agilent 6545 Q-ToF MS equipped with Agilent 1260 Infinity II Bio-inert Multsampler, Bio-inert Column compartment, bio-inert Quat. Pump, and DAD MW system. About 2 μL (25 uM solution diluted from 10 mM DMSO stock with acetonitrile supplemented with 0.1% formic acid) of each compound was injected into Waters Xselect C18 CSH 3.5u, 2.1mm ID x 30mm column. The pump flow rate was 0.8 mL/min. Buffer A is 10 mM NH4AC in 99% water, 1% acetonitrile (in house supply). Buffer B is 10 mM NH4AC in 5% water, 95% acetonitrile (in house supply).The gradient was set as follows: 0 min, 0% buffer B; 0.5 min, 0% buffer B; 2.0 min, 100% buffer B; 2.5 min, 100% buffer B; 2.51 min, 0% buffer B, and 3.0 min, 0% buffer B. The compounds were ionized using a Dual Jet Stream Electric Spray Ionization with VCap 4.5 kV voltage and nozzle 2.0 kV voltage. The mass spectrometer was set to acquire masses from 0 to 1700 D in positive mode. MS/MS spectra of each compound

were also acquired under Agilent MassHunter Workstation Data Acquisition and Agilent MassHunter Qualitative Analysis to confirm the chemical structure of the compounds.

Solubility of each compound in pH 6.8 phosphate buffer was determined using a nephelometer to determine the turbidity of the solution. Compounds were dissolved in DMSO at 10 mM and then serially diluted in phosphate buffer using a Tecan liquid handling system and the Gemini software system. Turbidity was measured using the LabSystems Nepheloskan Ascent instrument and solubility was determined using the Ascent software system from LabSystems.

Biological methods

Proteasome purification

Synchronized late-stage 3D7 parasites (~10% parasitaemia) were harvested by saponin lysis (0.05% w/v in PBS), then washed twice with diluted saponin (0.0025% w/v in PBS) and in PBS until the supernatant was clear. Harvested pellets were stored at -80°C until needed. Several pellets from consecutive weeks were used for purification (equating to ~6-10 L of initial culture). *P. falciparum* proteasome enrichment used in the enzyme assays was generated as previously described (4). The 20S proteasome was highly purified with additional chromatographic steps for the cryo EM studies (9). Human proteasome and human proteasome activator complex, PA28αβ, were prepared as described previously (12).

Proteasome activity assays

For *Pf* 20S assays, we used fluorogenic substrate Ac-nLPnLD-AMC for caspase-like (β1) activity, Ac-WLR-AMC for trypsin-like (β2) activity and Ac-WLA-AMC for chymotrypsin-like (β5) activity. Two buffer systems were used to examine the effect of inhibitors against the proteasome. The HEPES buffered condition consists of 20 mM HEPES pH 7.4, 0.5 mM EDTA, 0.01% BSA. The Tris buffered condition consists of 50 mM Tris pH 7.4, 5 mM MgCl$_2$, 1 mM DTT, 0.01% BSA. Compounds were firstly added to black 96-well plates with 3-fold dilutions from the low micromolar range. Other components in the reaction mixture included 15 μM substrates, 20 nM human PA28 αβ and 1 nM *Pf*20S or 0.15 nM *Hs*20S. The reaction was incubated at 37°C for 1 h and the increase in fluorescence was measured in a microplate reader (FLUOstar, BMG-LABTECH). IC$_{50}$ values were calculated by nonlinear regression of the background-corrected florescence values, *F*, on inhibitor concentration, *[I]*, using a four-parameter logistic equation:

Equation 1.

$$F = \frac{max - min}{1 + \left(\frac{IC_{50}}{[I]}\right)^h} + min$$

h is the Hill slope, *max* is the upper plateau (with uninhibited enzyme), and *min* is the plateau fluorescence at high inhibitor concentration (with completely inhibited enzyme). For the inhibition of *Pf*20S β5 active site by β5 selective inhibitors, hydrolysis of the substrate Ac-WLA-AMC by the β2 active site of *Pf*20S results in estimates of *min* of approximately 20% of the max value. The *min* is approximately zero for all the other

assays. Inhibitory effects of the compounds against the β1 and β2 active sites were examined using the Tris buffer system.

For Hs20S constitutive proteasome (Boston Biochem) assays, Z-LLE-AMC was used for β1c activity, Ac-KQL-AMC was used for β2c activity and Ac-WLA-AMC was used for β5c activity. For Hs20S immunoproteasome (Boston Biochem) assays, Ac-PAL-AMC was used for β1i activity, Ac-KQL-AMC was used for β2i activity and Ac-ANW-AMC was used for β5i activity, as previously described (13).

Progress curve analysis

Progress curves for hydrolysis of Ac-WLA-AMC were used to estimate the kinetic parameters (K_i, k_{on}, k_{off}) for compounds binding to the β5 active sites of Pf20S and Hs20Sc proteasomes. Production of free AMC was measured with a Cary Eclipse fluorescence spectrophotometer equipped with a thermostated 4 position cell holder. Reactions were prepared in cuvettes containing 2 mL of 20 mM HEPES pH 7.4, 0.5 mM EDTA, 0.01% BSA at 37°C with continuous stirring. The substrate, Ac-WLA-AMC was used at K_M (24 μM for Hs20Sc and 40 μM for Pf20S) and the enzyme concentration used was used at 1 nM for Pf20S or 0.15 nM for Hs20Sc. Both enzymes were activated with a saturating concentration (20 nM) of human PA28αβ activator. The uninhibited reaction velocity (v_o) was estimated as the slope of the progress curve before addition of inhibitor. After inhibitor was added, the progress curves were monitored for 90 min. The fluorescence ($F \sim$ free [AMC]) vs time (t) data were fit to equation 2 to derive values for the final steady-state inhibited velocities (v_i) and the rate constants for approach to steady-state, k_{obs}.

Equation 2.
$$F = v_i t + \frac{v_o - v_i}{k_{obs}}[1 - exp(-k_{obs}t)]$$

Fractional velocity (v_i/v_o) vs inhibitor concentration were fit to equation 3a (Hs20Sc) or equation 3b (Pf20S) to derive estimates for the K_{iapp} values. Equation 3b assumes a constant background hydrolysis of Ac-WLA-AMC in the Pf20S β2 active site estimated at 14% of the total uninhibited reaction velocity based on the data in Figure S2c.

Equation 3a.
$$\frac{v_i}{v_0} = \frac{1}{1 + \frac{[I]}{K_{iapp}}}$$

Equation 3b.
$$\frac{v_i}{v_0} = \frac{0.86}{1 + \frac{[I]}{K_{iapp}}} + 0.14$$

The slow binding inhibition was modelled as a simple bimolecular reaction (in competition with substrate) according to equation 4 to calculate the kinetic parameters in Table S4.

Equation 4.
$$k_{obs} = \frac{k_{off}}{K_{iapp}}[I] + k_{off}$$

Labelling of proteasome catalytic subunits with BMV037

BMV037 was prepared as previously described (4). Purified *Pf*20S proteasome (100 nM) was incubated with 10 µM boronate compounds at 37°C for 2 h. Treated *Pf*20S was labelled with BMV037 (10 µM) at 37°C for 2 h. Samples were mixed with SDS loading buffer, heated at 95°C for 5 min and applied to a 4–12% Bis-Tris acrylamide gel using MES SDS running buffer (Thermo Fisher Scientific). Gels were imaged using the Cy5 channel on a Gel Doc XR+ Documentation System (Bio-Rad).

Assessment of activity against 3D7 P. falciparum

Sorbitol-treated ring stage parasites were incubated with the inhibitors for 72 h and viability was assessed in the second cycle (14). Drug pulse assays were performed as described previously (15). Briefly, sorbitol synchronized ring stage parasites at 0.2% hematocrit and 1-2% parasitemia were incubated with an inhibitor dilution series at 37°C until parasites reached trophozoite stage of the following cycle. Cells were then stained with 2 µM Syto-61 (Thermo Fisher Scientific) and their fluorescence measured by flow cytometry (FACSCanto™ II cytometer; Becton Dickinson). Data were gated and analysed using FCS Express software (version 3) to determine the parasitemia. Viability represents the parasitemia normalized to untreated and "kill-treated" controls, where "kill-treated" refers to samples treated with 2 µM DHA for 48-72 h.

For the interaction assays, DHA and MPI-5 were serially diluted in the presence of the other compound. Equal volumes (50 µL) were transferred to a new plate to generate the DHA/MPI-5 matrix. Controls comprised individual serial dilutions of DHA and the proteasome inhibitor. Tightly synchronized parasites (1-1.5% parasitemia, 0.2% final hematocrit) were added to the plates and incubated for 3 h. Drugs were removed and the parasitemia assessed in the trophozoite stage of the next cycle.

Mammalian toxicity screening

HepG2 (Human Caucasian hepatocyte carcinoma, HPACC cat.no. 85011430) cells were used as indicators for general mammalian cell toxicity using a previously described protocol (16). Briefly, cells were plated and incubated overnight to allow them to adhere as monolayers. A working stock of each test compound was transferred to an intermediate 384-well plate and pre-diluted with minimum essential media (MEM). The pre-diluted stocks were then transferred onto the cell monolayers, and the plates were incubated for 68 h. Resazurin (50 µM) was added to each well for 3 h and fluorescence was monitored (λ_{ex} = 528 nm, λ_{em} = 590 nm). A standard reference compound, doxorubicin, was included on all plates to monitor the quality of the assay (potency range 200-400 nM). Alternatively, the cytotoxic effect of the test compounds was evaluated on the HepG2 cell line procured from ATCC (American Type Culture Collection, Manassas, USA) using the Cell

Titer-glo luminescent cell viability assay reagents (Promega, catalog number: G7570) following the manufacturer's instructions.

Parasite reduction rate (PRR) analysis

PRR was assessed using a standardized method (17). The $IC_{50(48h)}$ for inhibition of MPI-11 was determined to be 98 nM using the *in vitro* ^{3}H-hypoxanthine incorporation assay. A culture of 10^5 3D7 (BEI resources) parasites was exposed to MPI-11 at 10 times the IC_{50} value. Aliquots of parasites were taken from the culture at 24 h and 48 h. Following treatment, the inhibitor was removed; and infected red blood cells were diluted using fresh red blood cells, previously labeled with the intracellular dye (carboxylfluorescein diacetate succinimidyl ester, CFDA-SE). Following a further 48-h incubation under standard conditions, the ability of treated parasites to establish infections in fresh labeled red blood cells was detected by two-color flow cytometry after labeling of parasite DNA. Controls containing untreated parasites were used.

Activity against panels of drug resistant P. falciparum and ex vivo field isolates of P. falciparum and P. vivax.

Compounds were assayed on nine *P. vivax* and seven *P. falciparum* isolates collected from mono-infected patients, who had signed a written informed consent form to participate in the study, using previously described methods (5). The parasitemia ranged from 2,090-13,246 parasites/μL for *P. vivax* and 2,100-22,434 parasites/μL for *P. falciparum* isolates. Artesunate and chloroquine were assayed in parallel as standard compounds. The analyses included only the isolates that were incubated for ≥ 40 h with the compounds.

Compounds were tested against a range of drug-resistant laboratory strains using a modified [^{3}H]-hypoxanthine incorporation assay, as previously reported (18).

Activity against transmissible stages of P. falciparum

Activity against male gametes was assessed using the dual gamete formation assay (*Pf*DGFA) (6). Compounds were incubated with mature stage V gametocytes for 48 h in 384 well plates before gamete formation was triggered by a drop in temperature and addition of xanthurenic acid. Male gamete exflagellation was recorded and quantified by automated microscopy.

Activity against P. berghei exoerythrocytic stages

Hepatic human transformed cells (HepG2) were pre-treated for 18 h with the compound of interest, then infected with freshly dissected luciferase-expressing *P. berghei* sporozoites. Following incubation for 48 h, the viability of *P. berghei* exoerythrocytic forms was measured by bioluminescence (19).

Primary human hepatocytes were cultured for 2 days and then overlaid with *P. falciparum* NF54 sporozoites and compounds. Supernatant was refreshed daily with fresh compounds. 4 days post-infection, hepatocytes were stained for the presence of liver stage parasites (8).

HepG2 cells infected with luciferase-expressing *P. berghei* sporozoites were seeded onto compound-loaded 384-well plates 2 h after sporozoite addition. A live luciferase readout at 48 h post infection (hpi) (20) provides information on compound activity against parasite growth, while high content imaging (HCI) of MSP1 and AMA1 expression at 72 hpi provides information on hepatic merozoite formation. Compound effect on

hepatocyte was assessed based on HepG2 area occupied in the 72 hpi HCI assay. All data points were normalized to in-plate DMSO controls.

P. falciparum resistance selection studies

Dd2 parasites were obtained from T. Wellems (NIAID, NIH) and cloned by limiting dilution to obtain Dd2-B2. Parasite survival was assessed by flow cytometry on an Accuri C6 (BD Biosciences) using SYBR Green and MitoTracker Deep Red (Life Technologies) as nuclear stain and vital dyes, respectively (21). The IC_{50} was determined to be 557 nM in Dd2-B2 (n = 3). Selections were performed across an inoculum range of 2E5 to 6E7 parasites, or a single inoculum of 2E9 parasites, and a concentration of 2.3 μM MPI-12. Resistant parasites were only obtained in the 2E9 inoculum and these were cloned by limiting dilution prior to phenotypic characterization and whole-genome sequence analysis. 72 h dose-responses assays were conducted as per (21), with parasitemias determined by flow cytometry on an Accuri C6 (Becton Dickinson) with SYBR Green and MitoTracker Deep Red-labeled parasites. IC_{50} values were determined by non-linear regression (Prism version 8).

The fitness of the Met45Ile mutant parasites relative to the parental Dd2-B2 line was assessed over period of 21 days, using a mixed culture competition assay (3). Mutant and parental parasites were separately cultured 1:1 with the Dd2-attB-GFP reporter line, and the relative percentage of eGFP+ cells was quantified by flow cytometry three times a week. Assays were conducted on two independent occasions each, with three technical replicates.

Whole-genome sequence analysis

Whole-genome sequencing was performed as previously described (22), with modifications. Briefly, libraries were prepared for the resistant clones and the sensitive Dd2-B2 parent, using the Illumina Nextera DNA Flex library prep kit with dual indices according to the manufacturer's protocol. Two μg of genomic DNA was sheared to mean fragment sizes of 550 bp, end-repaired, adenylated on 3′ ends, and ligated with adaptors. The samples were pooled and multiplexed on a MiSeq flow cell to generate 2 × 300 bp paired end reads. Sequence data were aligned to the *P. falciparum* 3D7 genome (PlasmoDB version 48) using BWA (Burrow-Wheeler Alignment). PCR duplicates and unmapped reads were filtered out using Samtools and Picard MarkDuplicate. The reads were realigned around indels using GATK RealignerTargetCreator and base quality scores were recalibrated using GATK BaseRecalibrator. GATK HaplotypeCaller (version 4.1.8) was used to identify all possible variants in clones. These variants were filtered based on quality scores (min base quality score $\geq$ 18, variant quality as function of depth QD > 1.5, mapping quality > 50 and read depth (depth of read > 5) to obtain high quality single nucleotide polymorphisms that were annotated using snpEFF. The list of variants from the resistant clones were compared against the Dd2-B2 parent to identify non-synonymous single nucleotide polymorphisms present exclusively in the resistant clones at > 80% alternate allele frequency. Copy number variation analysis was performed using the BicSeq (23) to discover copy number variants (CNVs) in the

resistant mutants against the Dd2-B2 parent using the Bayesian statistical model. IGV (Integrated Genome Viewer, Broad Institute) was used to confirm the SNPs and CNVs present in the resistant clones.

P. falciparum humanized NOD-scid IL2Rnull mouse model

The model using *P. falciparum Pf3D7*[0087/N9] in NODscidIL2Rγ[null] mice engrafted with human red blood cells was adapted from a previously described procedure (24). Briefly, two engrafted mice/dosing group were infected intravenously with 2 x 10^7 *P. falciparum* (*Pf3D7*[0087/N9]) on day 0. The antimalarial efficacy was assessed following administration of one oral (p.o.) dose (50 mg/kg) of compound per day for four consecutive days on day 3, 4, 5 and 6 post-infection (4 x 50 mg/kg in total) and measuring the effect on blood parasitemia by microscopic analysis of Giemsa-stained blood smears (on days 3, 4, 5, 6 and 7 post-infection). Mice were euthanized on day 7.

Plasma exposure in mouse model

Compound was administered orally to two mice at 25 mg/kg on days 3, 4, 5, 6 after infection. On day 3, blood samples (20 µL) were obtained at time points up to 24 h after the first administration. Protein was precipitated with acetonitrile and remaining compound was assessed by LC-MS/MS in the selected reaction monitoring mode using HESI ionization in positive ion mode.

In vitro liver microsomal metabolism study and cellular permeability studies.

Metabolic stability was assessed by incubating compounds in the presence of human (H) and rat (R) S9 liver fractions (Xenotech, Kansas USA). Liver S9 (LS9) incubations were conducted with 100 mM phosphate buffer, 2.5 mg/mL of LS9, 2 mM NADPH, 2.5 mM UDPGA, 3 mM MgCl$_2$, alamethicin and 1 µM test article totaling 80 µL in incubation volume. All the reagents, except the LS9 were mixed together and aliquoted (60 µL) into 96 well plates. The reaction was initiated with LS9 (20 µL). At time 0, 4, 12 and 30 min, the reactions were terminated with the addition of acetonitrile-containing carbutamide (as an internal standard). The terminated samples were then centrifuged to pellet the protein and the supernatant was injected onto an LC/MS. The test article was monitored for loss over time and the $t_{1/2}$ was determined. The calculated half-life was then used as described below to determine the EH (hepatic extraction ratio) for both human and rat.

Equation 5

$CL_{int} = (0.693 / t_{1/2}$ in vitro$) \times$ (mL incubation volume /mg S9) $\times$ (x mg of S9 / gram of liver) $\times$ (120 g of liver / kg of body weight)

Where:

X = 21.4 for human and 40 for rats

CL_{int} = intrinsic clearance

S9 = liver S9 fraction

$t_{1/2}$ = half-life

CL_h was calculated based on the intrinsic clearance values, which were converted to CL_h by normalizing to liver blood flow rate (Q) using Equation 6 (25-27).

Equation 6

$CL_h = Q \times CL_{int} / Q + CL_{int}$

Where:

CL_h = hepatic clearance

CL_{int} = intrinsic clearance (calculated from microsomal or S9 incubations)

Q = liver blood flow rate = 1.24 L/hr/kg for human and 4.8 L/hr/kg for rats

The E_h was calculated by dividing the CL_h by Q, as shown in Equation 7 (25-27).

Equation 7

$E_h = CL_h / Q$

Where:

E_h = hepatic extraction ratio

CL_h = hepatic clearance

Q = 1.24 L/hr/kg for human and 4.8 L/hr/kg for rats.

Caco-2 cells were cultured in Dubecco's Modified Eagle's Medium (DMEM) containing 10% Fetal Bovine Serum (FBS), 0.1 mM non-essential amino acids, 2 mM L-glutamine, 4.5g/L glucose, 25 mM HEPES. Cells were seeded onto 24-Transwells plate (0.33 cm^2/well, 0.4 mm pore size, Costar) at an initial density of 10^5 cells/well and incubated at 37°C in an atmosphere of 5% CO_2 in air and 90% humidity. The medium containing 10% FBS was changed every other day. The cells were cultured for 21-25 days to differentiate them into enterocyte-like cells. The transepithelial electrical resistance (TEER) was measured to ensure tight junction formation and cells with TEER value more than 250 ohms.cm^2 were used in the study. On the day of the transport study, cells were washed with warm HBSS buffer and equilibrated with buffer for 60 min. Test article at a concentration of 5 μM (containing 50 μM Lucifer Yellow) was added in 24 Transwell cell plate (apical 210 μL and basal 1000 μL) and buffer was added in the receiver side (apical 200 μL and basal 1000 μL). 10 μL sample from donor side was aliquoted for recovery measurement. Cells were incubated at 37°C for 60 min and 120 μL samples were aliquoted from the receiver side at 30 and 60 min. Samples were mixed with 100 nM carbutamide in acetonitrile (ACN) containing 0.1% formic acid (internal standard). Samples were centrifuged at 2056 x g for 10 min and the supernatant was collected and analyzed for quantification of the test article by LC-MS.

Rat pharmacokinetics (PK) analyses

Citrate esters of selected compounds (MPI-11, MPI-5, MPI-10, MPI-13; HCl salts) were formulated in 10% hydroxypropyl-β-cyclodextrin and administered to male Sprague-Dawley rats at 1 mg/kg by intravenous and oral administration (n = 2 per route of administration at 1 and 5 mL/kg). Blood was collected from a jugular cannula at 0.083, 0.25, 0.5, 1, 2, 4, 8 and 24 h post IV dosing and at the same times (except the 0.083-h sample following oral administration) and then processed into plasma. Blood samples were also retained at 1 h post IV dosing for estimation of red blood cell partitioning and urine was collected 24 h post-dosing for the

determination of the percentage of the administered dose recovered in 0-24 h urine as unchanged parent. Samples were precipitated with 0.5% formic acid in methanol and the supernatants were analyzed by positive ion electrospray LC-MS for the administered compound. Non-compartmental pharmacokinetic parameters were calculated from individual concentration vs time profiles using Phoenix 64 (WinNonlin) Version 8.1 Certara, Princeton NJ.

Preparation of samples for cryoEM data acquisition

Two 2.8 µL aliquots of *Pf*20S or *Hs*20Sc (0.15 mg/mL) solution were incubated for 1 h at 37°C in the presence of 0.1 µL bortezomib or compound MPI-5, respectively. The final concentration of both drugs was made up to 10 μM. Following incubation, *Pf*20S aliquots were treated with 0.1 µL glutaraldehyde (final concentration 0.1% v/v), snap frozen in liquid nitrogen and stored at -80°C until use. *Hs*20Sc was purchased from Boston Biochem (catalogue number E-360).

CryoEM data acquisition and reconstruction

Samples were applied to glow-discharged (25 mA for 30 sec) UltrAuFoil® R1.2/1.3 300 mesh grids (Quantifoil). Humidity and temperature were kept constant at 100% and 4°C using a Vitrobot Mark IV (FEI). The grids were plunge-frozen in liquid ethane and loaded into a Talos Arctica cryoTEM (ThermoFisher) operating at 200 kV. Images were recorded on a K2 Summit direct electron detector (Gatan) in counting or super-resolution mode with the microscope operating in Energy Filtered TEM (EFTEM) mode using the GIF BioQuantum Energy Filter (Gatan). The images were taken using EPU automation software (FEI) at a nominal magnification of 100,000x, in EFTEM mode, yielding a pixel size of 1.31 Å in counting mode or 0.655 Å in super-resolution mode. Each movie was recorded over 40 frames with a total dose of 50 to 64 e$^-$/Å^2. For data acquisition statistics, see Table S10.

The movies were motion-corrected in the Relion 3.1 pipeline (28, 29) using MotionCor 2 (30) and the CTF determined by gCTF (31). Motion-corrected movies were exported to CryoSparc for particle picking and 2D class averaging (typically 2 rounds of 2D class averaging). Particles were imported into Relion using PyEM (32). A *de novo* model was created for each dataset, this model was then refined, ctf-refined and polished. Polished particles were then imported in CryoSparc for final refinement.

Model building and refinement

The map was sharpened using *phenix.autosharpen* prior to refinement. For the two *Pf*20S structures, our previously-deposited model of *Pf*20S (PDB: 6MUW)(9) was fit into the density using *Chimera* (33). Real-space refinement was conducted in Phenix 1.18 (34, 35), using *phenix.real_space_refine*, with non-crystallographic symmetry (NCS) constraints and Ramachandran restraints. Manual coordinate corrections were made using *COOT* (36). No reference model restraints were used for the *Pf*20S structures. Map-model fit and geometry validation were performed in *Phenix* 1.18, incorporating *MOLProbity* (11, 34, 37).

A model of the *Pf*20S Met45Ile mutant was constructed using *COOT* (36) by replacing Met45 with the top populated Ile rotamer. Restraints for bortezomib and MPI-5 were generated using MOPAC7.1 (38) including

restraints for the threonine hydroxyl-boron bond. The improved resolution of these structures allowed us to correct several register issues with the previously-deposited *Pf*20S structures (9, 39).

For the *Hs*20Sc/MPI-5 structure, the structure was refined essentially as described for the *Pf*20S structures, using a previously-solved high-resolution structure of the apo-*Hs*20Sc structure (PDB: 5LE5) (40), and using the restraints generated for MPI-5. For the *Hs*20Sc/MPI-5 structure, reference model restraints were applied in *phenix.real_space_refine*, using the high-resolution structure as a reference model (35, 40). For model building and refinement statistics, see Table S10.

SI References

1. Zmuda F*, et al.* (2019) Identification of novel *Trypanosoma cruzi* proteasome inhibitors using a luminescence-based high-throughput screening assay. *Antimicrob Agents Chemother* 63(9).
2. Kirkman LA*, et al.* (2018) Antimalarial proteasome inhibitor reveals collateral sensitivity from intersubunit interactions and fitness cost of resistance. *Proc Natl Acad Sci U S A* 115(29):E6863-E6870.
3. Ross LS*, et al.* (2018) Emerging Southeast Asian PfCRT mutations confer *Plasmodium falciparum* resistance to the first-line antimalarial piperaquine. *Nat Commun* 9(1):3314.
4. Xie SC*, et al.* (2018) Target validation and identification of novel boronate inhibitors of the *Plasmodium falciparum* proteasome. *J Med Chem* 61(22):10053-10066.
5. Aguiar AC, Pereira DB, Amaral NS, De Marco L, & Krettli AU (2014) *Plasmodium vivax* and *Plasmodium falciparum ex vivo* susceptibility to anti-malarials and gene characterization in Rondonia, West Amazon, Brazil. *Malar J* 13:73.
6. Delves MJ*, et al.* (2018) A high throughput screen for next-generation leads targeting malaria parasite transmission. *Nature Communications* 9(1):3805.
7. Swann J*, et al.* (2016) High-throughput luciferase-based assay for the discovery of therapeutics that prevent malaria. *ACS Infect Dis* 2(4):281-293.
8. Schalkwijk J*, et al.* (2019) Antimalarial pantothenamide metabolites target acetyl-coenzyme A biosynthesis in *Plasmodium falciparum*. *Science translational medicine* 11(510).
9. Xie SC*, et al.* (2019) The structure of the PA28-20S proteasome complex from *Plasmodium falciparum* and implications for proteostasis. *Nat Microbiol* 4(11):1990-2000.
10. Schneider TR, Stark H, Bourenkov G, & Chari A (2016) The inhibition mechanism of human 20S proteasomes enables next-generation inhibitor design. *Science* 353:594-598.
11. Williams CJ*, et al.* (2018) MolProbity: More and better reference data for improved all-atom structure validation. *Protein Science* 27:293-315.
12. Williamson MJ*, et al.* (2006) Comparison of biochemical and biological effects of ML858 (salinosporamide A) and bortezomib. *Mol Cancer Ther* 5(12):3052-3061.
13. Blackburn C*, et al.* (2010) Characterization of a new series of non-covalent proteasome inhibitors with exquisite potency and selectivity for the 20S beta5-subunit. *The Biochemical journal* 430(3):461-476.
14. Dogovski C*, et al.* (2015) Targeting the cell stress response of *Plasmodium falciparum* to overcome artemisinin resistance. *PLoS Biol* 13(4):e1002132.
15. Xie SC, Dogovski C, Kenny S, Tilley L, & Klonis N (2014) Optimal assay design for determining the in vitro sensitivity of ring stage *Plasmodium falciparum* to artemisinins. *Int J Parasitol* 44(12):893-899.
16. Baragana B*, et al.* (2019) Lysyl-tRNA synthetase as a drug target in malaria and cryptosporidiosis. *Proc Natl Acad Sci U S A*.
17. Linares M*, et al.* (2015) Identifying rapidly parasiticidal anti-malarial drugs using a simple and reliable *in vitro* parasite viability fast assay. *Malaria Journal* 14(1):441.

18. Snyder C, Chollet J, Santo-Tomas J, Scheurer C, & Wittlin S (2007) *In vitro* and *in vivo* interaction of synthetic peroxide RBx11160 (OZ277) with piperaquine in Plasmodium models. *Exp Parasitol* 115(3):296-300.

19. Swann J*, et al.* (2016) High-throughput luciferase-based assay for the discovery of therapeutics that prevent malaria. *ACS infectious diseases* 2(4):281-293.

20. Van Voorhis WC*, et al.* (2016) Open source drug discovery with the Malaria Box compound collection for neglected diseases and beyond. *PLoS pathogens* 12(7):e1005763.

21. Ekland EH, Schneider J, & Fidock DA (2011) Identifying apicoplast-targeting antimalarials using high-throughput compatible approaches. *FASEB J* 25(10):3583-3593.

22. Vanaerschot M*, et al.* (2020) Inhibition of resistance-refractory *P. falciparum* kinase PKG delivers prophylactic, blood stage, and transmission-blocking antiplasmodial activity. *Cell chemical biology* 27(7):806-816.e808.

23. Xi R*, et al.* (2011) Copy number variation detection in whole-genome sequencing data using the Bayesian information criterion. *Proc Natl Acad Sci U S A* 108(46):E1128-1136.

24. Jiménez-Díaz MB*, et al.* (2009) Improved murine model of malaria using *Plasmodium falciparum* competent strains and non-myelodepleted NOD-scid IL2R gamma-null mice engrafted with human erythrocytes. *Antimicrobial agents and chemotherapy* 53(10):4533-4536.

25. Shimada T, Yamazaki H, Mimura M, Inui Y, & Guengerich FP (1994) Interindividual variations in human liver cytochrome P-450 enzymes involved in the oxidation of drugs, carcinogens and toxic chemicals: studies with liver microsomes of 30 Japanese and 30 Caucasians. *J Pharmacol Exp Ther* 270(1):414-423.

26. Guengerich FP (1999) Cytochrome P-450 3A4: regulation and role in drug metabolism. *Annual review of pharmacology and toxicology* 39:1-17.

27. Davies B & Morris T (1993) Physiological parameters in laboratory animals and humans. *Pharm Res* 10(7):1093-1095.

28. Zivanov J*, et al.* (2018) New tools for automated high-resolution cryo-EM structure determination in RELION-3. *Elife* 7.

29. Scheres SH (2015) Semi-automated selection of cryo-EM particles in RELION-1.3. *J Struct Biol* 189(2):114-122.

30. Zheng SQ*, et al.* (2017) MotionCor2: anisotropic correction of beam-induced motion for improved cryo-electron microscopy. *Nat Methods* 14(4):331-332.

31. Zhang K (2016) Gctf: Real-time CTF determination and correction. *J Struct Biol* 193(1):1-12.

32. Asarnow D, Palovcak E, & Cheng Y (2019) UCSF pyem v0.5. Zenodo doi:10.5281/zenodo.3576630.

33. Pettersen EF*, et al.* (2004) UCSF Chimera--a visualization system for exploratory research and analysis. *J Comput Chem* 25(13):1605-1612.

34. Adams PD*, et al.* (2010) PHENIX: A comprehensive Python-based system for macromolecular structure solution. *Acta Crystallographica Section D: Biological Crystallography* 66:213-221.

35. Afonine PV*, et al.* (2018) Real-space refinement in Phenix for cryo-EM and crystallography. *Acta Crystallographica Section D Structural Biology* 74:531-544.

36. Emsley P, Lohkamp B, Scott WG, & Cowtan K (2010) Features and development of Coot. *Acta Crystallogr D Biol Crystallogr* 66(Pt 4):486-501.

37. Prisant MG, Williams CJ, Chen VB, Richardson JS, & Richardson DC (2020) New tools in MolProbity validation: CaBLAM for CryoEM backbone, UnDowser to rethink "waters," and NGL Viewer to recapture online 3D graphics. *Protein Science* 29:315-329.

38. Stewart JJ (1990) MOPAC: a semiempirical molecular orbital program. *Journal of computer-aided molecular design* 4(1):1-105.

39. Li H*, et al.* (2016) Structure and function based design of Plasmodium-selective proteasome inhibitors. *Nature* 530:233–236.

40.   Schrader J*, et al.* (2016) The inhibition mechanism of human 20S proteasomes enables next-generation inhibitor design. *Science* 353(6299):594-598.